JOURNAL OF PETROLOGY | VOLUME 48 | NUMBER 7 | PAGES 1321–1349 | 2007 | doi:10.1093/petrology/egm020

The Proterozoic *P–T–t* Evolution of the Kemp Land Coast, East Antarctica; Constraints from Si-saturated and Si-undersaturated Metapelites

J. A. HALPIN[1]*, R. W. WHITE[2,3], G. L. CLARKE[1] AND D. E. KELSEY[4]

[1]SCHOOL OF GEOSCIENCES, UNIVERSITY OF SYDNEY, SYDNEY, NSW 2006, AUSTRALIA

[2]SCHOOL OF EARTH SCIENCES, UNIVERSITY OF MELBOURNE, MELBOURNE, VIC 3010, AUSTRALIA

[3]PRESENT ADDRESS: INSTITUTE OF GEOSCIENCE, UNIVERSITY OF MAINZ, D-55099 MAINZ, GERMANY

[4]CONTINENTAL EVOLUTION RESEARCH GROUP, SCHOOL OF EARTH & ENVIRONMENTAL SCIENCES, UNIVERSITY OF ADELAIDE, ADELAIDE, SA 5005, AUSTRALIA

RECEIVED JUNE 29, 2006; ACCEPTED MARCH 29, 2007

Integrated metamorphic and geochronological data place new constraints on the metamorphic evolution of a Neoproterozoic orogen in east Antarctica. Granulite-facies rocks from a 150 km stretch of the Kemp Land coast reflect peak conditions involving $T \approx 870$–$990^{\circ}C$ at $P \approx 7{\cdot}4$–10 kbar, with pressure increasing westward towards an Archaean craton. Electron microprobe-derived (Th + U)–Pb monazite ages from metapelitic assemblages indicate that the major mineral textures in these rocks developed during the c. 940 Ma Rayner Orogeny. Complex compositional zoning in monazite suggests high-T recrystallization over c. 25 Myr. Diversity in metapelitic reaction textures reflects silica and ferromagnesian content: Si-saturated Fe-rich metapelites contain garnet that is partially pseudomorphed by biotite and sillimanite, whereas Si-saturated Mg-rich metapelites and Si-undersaturated metapelitic pods have reaction microstructures involving cordierite enclosing orthopyroxene, garnet and/or sapphirine, cordierite + sapphirine symplectites around sillimanite and coarse-grained orthopyroxene + corundum separated by sapphirine coronae. Interpretations based on P–T pseudosections provide integrated bulk-rock constraints and indicate a clockwise P–T–t path characterized by a post-peak P–T trajectory with $dP/dT \approx 15$–20 bar/$^{\circ}C$. This moderately sloped decompressive-cooling P–T path is in contrast to near-isothermal decompression P–T paths commonly cited for this region of the Rayner Complex, with implications for the post-collisional tectonic response of the mid- to lower crust within this orogenic belt.

KEY WORDS: *electron microprobe monazite dating; granulite facies; Rayner Complex; sapphirine; THERMOCALC*

Minerals abbreviations: q, quartz; g, garnet; sill, sillimanite; ky, kyanite; opx, orthopyroxene; cd, cordierite; ksp, alkali feldspar; pl, plagioclase; bi, biotite; sp, spinel; ilm, ilmenite; mt, magnetite; ru, rutile; sa, sapphirine; cor, corundum; osm, osumilite; liq, silicate melt; mnz, monazite

INTRODUCTION

Characterization of the metamorphic history for middle to lower crustal rocks is largely based on the interpretation of mineral reaction microstructures. However, different *P–T* paths may produce the same observed texture in a given rock, and vice versa a mineral reaction microstructure does not uniquely define a *P–T* path (e.g. Vernon, 1996; Kelsey *et al.*, 2003*b*). Furthermore, the inferred *P–T* trajectory is valid only if all the metamorphic reaction textures developed during the same event (e.g. Hand *et al.*, 1992; Vernon, 1996; Goncalves *et al.*, 2004). The calculation of *P–T* pseudosections as a technique for deciphering *P–T* paths is becoming increasingly common as sophisticated thermodynamic datasets become available for chemical systems that closely approximate actual rock compositions. Many workers have successfully used *P–T* pseudosections to constrain prograde and retrograde

*Corresponding author. Telephone: +61 2 93512919. Fax: +61 2 93510184. E-mail: jacqui.halpin@mac.com

paths via the calculation of mineral mode contours (e.g. Stüwe & Powell, 1995; White *et al.*, 2002; Boger & White, 2003; Johnston *et al.*, 2003; Kelsey *et al.*, 2003*c*, 2005; Ouzegane *et al.*, 2003; Zeh *et al.*, 2004). In this way mineral reaction microstructures involving the production of one or more minerals at the expense of an earlier mineral assemblage can be quantified, and a P–T trajectory would cross modal contours representative of such a reaction. Integrated with geochronological data and a structural context, this approach provides a powerful means for the estimation of P–T–t paths.

This paper investigates the Proterozoic P–T–t evolution of a reworked Archaean terrane exposed along the Kemp Land coastline in east Antarctica. Granulite-facies rocks in this area record evidence of the large-scale, *c.* 1000–900 Ma, Rayner Orogeny (locally known as the Rayner Structural Episode: Sandiford & Wilson, 1984) induced by the convergence of the Napier Complex and parts of the Indian Peninsula, with a continental block that now constitutes much of east Antarctica (e.g. Mezger & Cosca, 1999). The thermo-physical evolution of the orogenic belt in this region of east Antarctica is still poorly understood; access to the area is difficult, extrapolation between ice-covered regions is necessary, and previous work has mostly relied on conventional thermobarometry (e.g. Ellis, 1983; Black *et al.*, 1987). Recent work (e.g. Kelly & Harley, 2004a) suggests a 'clockwise' P–T path and near-isothermal decompression (ITD) from high to ultra-high temperatures in rocks from western Kemp Land during the Neoproterozoic. In this study we estimate peak P–T conditions and the post-peak evolution of the Kemp Land rocks via modelling of the mineralogical evolution of a suite of metapelitic assemblages from the Stillwell Hills, Broka and Havstein Islands and the Oygarden Group, three locations that constitute the most accessible outcrop along the Kemp Land coast (Fig. 1). Si-saturated (quartz-present) gneisses provide 'peak' P–T estimations via pseudosections calculated in the system Na_2O–CaO–K_2O–FeO–MgO–Al_2O_3–SiO_2–H_2O–TiO_2–Fe_2O_3 (NCKFMASHTO). The trajectory of the P–T path for rocks from the Stillwell Hills is constrained via the interpretation of several stages of sapphirine growth and associated reaction textures in Si-undersaturated (quartz-absent) metapelites, combined with the constraints from post-peak assemblages in Si-saturated assemblages. Finally, the timing of the inferred metamorphic evolution is constrained by *in situ* electron microprobe (EMP) dating of coexisting monazite grains. This 'bulk rock integrated' approach incorporates constraints from diverse metamorphic assemblages and allows for a well-constrained P–T–t path for Neoproterozoic orogenesis in the Stillwell Hills. This revised metamorphic evolution may be more widely applicable to the Kemp Land terrane with implications for the thermo-physical evolution of this region of the East Antarctic Shield.

REGIONAL GEOLOGY

Granulite-facies rocks in Kemp Land, together with those exposed in parts of Enderby Land (to the west) and MacRobertson Land (to the east), constitute the greater Rayner Complex in east Antarctica, originally defined as distinct from the Napier Complex in Enderby Land by Kamenev (1972; Fig. 1). Archaean components of Kemp Land are preserved in the Stillwell Hills, Broka and Havstein Islands and the Oygarden Group (Fig. 1; Clarke, 1988; Kelly *et al.*, 2004; Halpin *et al.*, 2005) and Hf model ages indicate a *c.* 3900–3600 Ma source, similar to model ages reported for parts of the Napier Complex (e.g. Rippon Point; Halpin *et al.*, 2005). At least part of Kemp Land is therefore Archaean cratonic material reworked during the Rayner Orogeny (e.g. Sheraton *et al.*, 1980, 1987; Grew *et al.*, 1988).

Effects of the Rayner Orogeny at *c.* 940–930 Ma in rocks along the Kemp Land coast (Grew *et al.*, 1988; Kelly *et al.*, 2002; Halpin *et al.*, 2005) have been interpreted to result from ductile thrusting of Archaean gneiss westward onto a craton, now represented by the Napier Complex (Clarke, 1988). A macroscopic strain gradient developed during the Rayner Orogeny increases to the east, recorded by metamorphosed basic dykes that cut Archaean foliations in extensive layered orthogneiss in Kemp Land (Stillwell Gneiss; Trail, 1970). Extensive *c.* 990–960 Ma charnockitic and felsic magmatism associated with the Rayner Orogeny, which post-date peak P–T conditions along the Mawson Coast in MacRobertson Land (Young & Black, 1991; Dunkley *et al.*, 2002), are not obvious in Kemp Land. Kelly *et al.* (2002) suggested this may be indicative of a two-stage structural evolution for the Rayner Complex during the Rayner Orogeny.

P–T data for rocks in western Kemp Land are limited. Estimates made by Black *et al.* (1987) in the Dismal Mountains (Fig. 1) yielded peak conditions of $T = 800$–850°C at $P = 5$–7 kbar. Ellis (1983) obtained estimates of $T = 700$–800°C at $P = 8{\cdot}4$–11 kbar from rocks at Turbulence Bluffs (Fig. 1a). Mafic granulites in western Kemp Land commonly contain plagioclase + orthopyroxene symplectites that enclose garnet; P–T estimates for these textures fall in the range $P = 3$–$5{\cdot}9$ kbar at $T = 660^\circ$C and have been interpreted to suggest partial equilibration at lower pressures (Ellis, 1983). P–T estimates based on mafic and metapelitic granulites from the Oygarden Group (Fig. 1) indicate peak or near-peak conditions of $P > 9$–10 kbar at $T = 800$–950°C (Kelly *et al.*, 2000; Kelly & Harley, 2004*a*), followed by near-ITD to $P \approx 5$ kbar (Kelly *et al.*, 2000; Kelly &

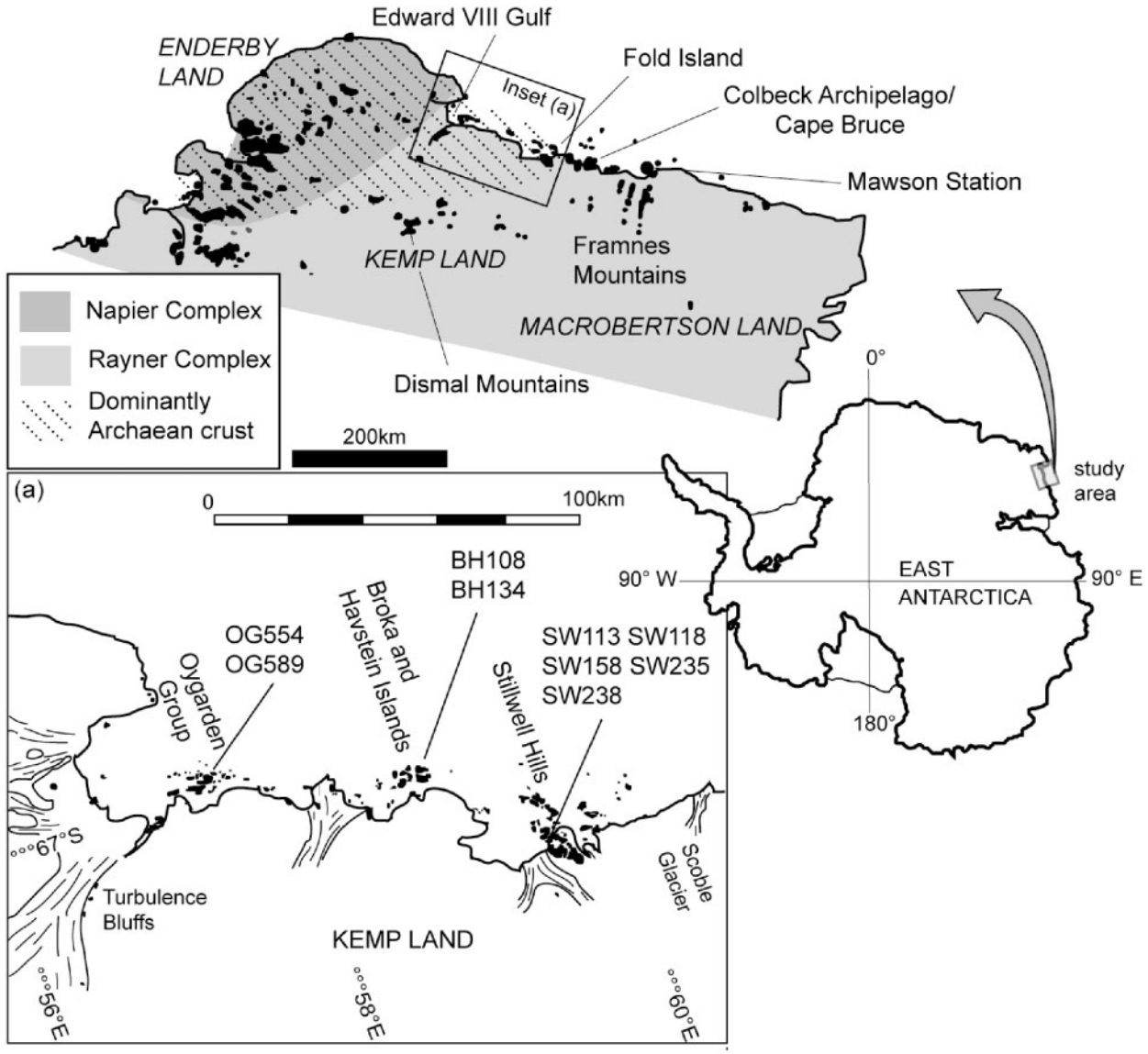

Fig. 1. The location of the Rayner and Napier Complexes in east Antarctica. Inset (a) shows localities along the Kemp Land coastline sampled in this study. Black areas indicate ice-free outcrops.

Harley, 2004*a*). Schröter (2006) modelled the mineralogical evolution of coronae in a mafic granulites from Broka and Havstein Islands (Fig. 1) and inferred peak P–T conditions of $P = 8{\cdot}4$ kbar at $T = 770^{\circ}$C followed by near-ITD to $P = 6 \pm 2$ kbar at $T = 750 \pm 50^{\circ}$C. Average P–T estimates for mafic assemblages made by Schröter (2006) suggest conditions of $P = 8{\cdot}4 \pm 1{\cdot}3$ kbar at $T = 760 \pm 90^{\circ}$C for the Stillwell Hills. These data suggest that a P–T path dominated by near-ITD characterizes the post-peak metamorphic evolution of Kemp Land, similar to P–T paths for the Rayner Complex in Enderby Land (reviewed by Harley & Hensen, 1990).

METAMORPHIC GEOLOGY

Outcrop setting

The layered Stillwell Gneiss dominates rock outcrop in Kemp Land west of the Scoble Glacier (Fig. 1), and forms extensive exposures in the Stillwell Hills, Broka and Havstein Islands and the Oygarden Group. The majority of this gneiss comprises alternating pyroxene–plagioclase-rich and quartz–feldspar-rich layers that record several high-grade deformation phases (Table 1: D_1–D_4 of Kelly *et al.*, 2000, 2002). Low-angle cross-cutting relationships between early felsic-dominated S_1 layers and

Table 1 Proposed deformational event correlations between prominent locations in Kemp Land

Kemp Land			
Oygarden Gp.	Broka & Havstein Is.	Stillwell Hills	Fold Island
(Kelly et al. 2000; Kelly et al. 2002; Kelly et al., 2004; this study)	(Halpin et al. 2005; J.A Halpin, unpub. data)	(*Clarke 1988; Halpin et al. 2005; J.A Halpin, unpub. data; this study)	(Grew et al. 1988; James et al. 1991)
> 3500 Ma protoliths to Stillwell Gneiss			
D1 ca. 3650 - 2780 Ma compositional layering and layer parallel foliation	D1 compositional layering and layer parallel foliation	D1 ? ca. 3400 Ma compositional layering and layer parallel foliation	D1 compositional layering and layer parallel foliation
> 2840 - 2780 Ma protolith to homogeneous felsic orthogneiss			
D2 ca. 2780 - 1600 Ma F2 isoclinal folds, transposition of S1 and post-D1 lithologies into S2	D2 F2 isoclinal folds, transposition of S1 and post-D1 lithologies into S2	D2 > 1550 Ma F2 isoclinal folds, transposition of S1 and post-D1 lithologies into S2	D2 F2 isoclinal folds, transposition of S1
		> 1550 Ma intrusion of charnockite	
ca. 1200 Ma mafic dykes (possible correlate with Amundsen dykes in Napier Complex)			
Rayner Orogeny			
D3a ca. 930 Ma high strain S3 and/or S3-composite high-grade foliation ductile low-angle thrusting F3a tight-isoclinal, recumbent & sheath folds, WSW-trending L3a//F3a, E-trending transport axis peak metm.	D3 ca. 940 Ma high strain S3 and/or S3-composite high-grade foliation F3 tight-isoclinal, inclined-recumbent, F3/L3 variable orientation peak metm.	D3 (D1*) ca. 940 Ma high strain S3 and/or S3-composite high-grade foliation F3 westward verging, tight-isoclinal, inclined-recumbent, N-NE-trending, rotating to E-trending L3// or perpend. to F3 W-trending transport axis peak metm.	D3 high strain F3 tight-isoclinal, variable orientation → ?
D3b high strain F3b open-isoclinal, upright-reclined, coaxial to F3a L3b//F3b intense strain partitioning	D4 moderate-high strain F4 open-tight, upright-inclined, NE-trending, NE-SW-plunging	D4 (D3*) moderate strain F4 westward verging, open-tight, upright-inclined, N-NE-trending, N-S-plunging	D4 moderate strain F4 tight-isoclinal, inclined macro. F4 overturned to NE, N-plunging, rectangular closure with SE-NW & E-W-trending axial planes
D4 ca. 925 Ma high strain E-W-trending, steeply S-dipping high strain zone F4//L4 steeply ESE-plunging	D5 moderate-high strain F5 open-tight, upright-inclined, NW-SE-trending, NW-SE-plunging	D5 (D2*) moderate strain F5 open-tight, upright-inclined, E-SE-trending, E-W-plunging	D5 moderate strain F5 open, upright, SE-trending, shallowly SE-plunging
pegmatites	pegmatites	pegmatites	→ ca. 940 Ma pegmatites

mafic layers defining S_2 are consistent with parts of the mafic layering originating from deformed post-S_1 mafic dykes (Clarke, 1988; James *et al.*, 1991). D_1–D_2 are interpreted to have occurred prior to the Rayner Orogeny (James *et al.*, 1991; Kelly *et al.*, 2000). In the Oygarden Group of islands, effects of the Rayner Orogeny are characterized by macroscopic recumbent F_3 folds and east-trending thrusts commonly localized on mafic dyke–gneiss contacts (Kelly *et al.*, 2000). Steeply dipping D_4 shear zones locally transposed earlier fabrics (Kelly *et al.*, 2000). At Broka and Havstein Islands and the Stillwell Hills, pervasive sub-horizontal, simple shear-dominated D_3 deformation produced inclined to recumbent structures and invariably transposed earlier fabrics (Table 1). Open to tight, upright to inclined folding characterizes later Rayner Orogeny deformation in these areas.

Subordinate metapelitic gneiss occurs as discontinuous lenses or pods in *c.* 3650 Ma Stillwell Gneiss in the Oygarden Group (zircon U–Pb minimum emplacement age; Kelly *et al.*, 2004). Similar relationships occur at Broka and Havstein Islands, where metapelitic gneiss is interlayered with *c.* 3540 Ma orthogneiss (zircon U–Pb minimum emplacement age; Halpin *et al.*, 2005). Field relationships differ in the Stillwell Hills, where a distinctive iron-stained metapelitic package, hereafter referred to as the rusty gneiss, is infolded with, but not cut by, *c.* 3490 Ma Stillwell Hills Orthogneiss (zircon U–Pb minimum emplacement age; Halpin *et al.*, 2005). Though the rusty gneiss is tentatively correlated with metapelitic gneiss exposed throughout MacRobertson Land (McLeod *et al.*, 1966), age relationships are unclear because of the pervasive overprint during the Rayner Orogeny.

Metapelitic mineral assemblages

The investigated rocks can be divided into two compositional groups based on their distinct bulk compositions: Si-saturated and Si-undersaturated metapelites. The Si-saturated rocks are further subdivided into Fe-rich (Assemblage I) rocks, which contain garnet and sillimanite, and Mg-rich (Assemblage II) rocks, which additionally contain cordierite and orthopyroxene. The descriptions below are based on observations from a large number of thin sections from the Stillwell Hills (SW- sample numbers), Broka and Havstein Islands (BH- sample numbers) and the Oygarden Group (OG- sample numbers). Particular reference is made to samples used in the phase diagram calculations and summary information is presented in Tables 2 and 3.

Petrography of Si-saturated metapelites

Assemblage I (samples SW113, SW118, BH108, OG554)

Coarse-grained assemblages. Garnet (1–8 mm across) is enveloped by prismatic sillimanite, with or without biotite, rutile and opaque minerals (Fig. 2a). Larger garnet porphyroblasts commonly contain inclusions of quartz, sillimanite, ilmenite, plagioclase and lesser biotite and rutile, whereas garnet grains in more Fe-rich samples may contain inclusions of spinel and magnetite (e.g. BH108). Elongate garnet grains have sillimanite inclusions defining an internal fabric that is commonly orientated parallel to

Table 2: Si-saturated metapelitic mineral assemblages

	Assemblage I (Fe-rich)				Assemblage II (Mg-rich)	
Sample	SW113	SW118	BH108	OG554	BH134	OG589
garnet	P	P	P	P	P	P
orthopyroxene	—	—	—	—	P	P, $R_{8,9}$
cordierite	—	—	—	—	$PR_{6,7}$	P?$R_{6,7,10}$
biotite	$I_{1,4}R$	$I_{1,4}R$	$I_{1,4}R$	I_1R	$I_{1,3,5}R$	$I_{1,3}$
plagioclase	—	PR_{11}	M	PI_1	PR_{11}	P?$R_{6,7}$
alkali feldspar	P	P	P	PI_1	P	
spinel	—	—	I_1P	—	—	—
ilmenite	PI_1	PI_1	PI_1R_{12}	—	—	—
magnetite	—	—	I_1R_{12}	—	—	—
rutile	PI_1	$PI_{1,4}$	—	PI_1	$PI_{1,5}$	M
sillimanite	$PI_{1,2,4}R$	$PI_{1,4}R$	$PI_{1,4}R$	PI_1	$PI_{1,5}R$	M
quartz	PI_1	PI_1	$PI_{1,4}$	PI_1	PI_1	PI_1

P, peak metamorphic assemblage; R, retrograde metamorphic assemblage; I, inclusion or prograde phase; M, minor occurrence. Subscripts: 1, inclusion in garnet; 2, inclusion in quartz; 3, inclusion in orthopyroxene; 4, inclusion in alkali feldspar; 5, inclusion in cordierite; 6, corona to garnet; 7, corona to orthopyroxene, 8, corona to biotite; 9, symplectite with cordierite; 10, symplectite with orthopyroxene; 11, exsolution in alkali feldspar; 12, associated with spinel.

the dominant external fabric (Fig. 2a). Small, idioblastic (≤0·3 mm) and inclusion-poor garnet may also occur. Perthite (≤1·5 mm across) is elongate and may have fine-grained inclusions of sillimanite, biotite or rutile. Plagioclase is common only in leucocratic segregations, where it occurs with alkali feldspar and quartz. Sample OG554 is an exception to this generalization, where both alkali feldspar and plagioclase (≤1 mm) occur in textural equilibrium with other coarse-grained minerals in the matrix including quartz, biotite, sillimanite and garnet.

Fine-grained assemblages. Fine-grained sillimanite occurs at garnet–garnet grain boundaries (Fig. 2b). Minor fine-grained sillimanite is also present on the margins of prismatic sillimanite (Fig. 2b). Fine-grained biotite rims garnet in strain shadows, or cuts S_3. Minor ilmenite is exsolved from biotite. Myrmekite is present at some feldspar grain boundaries.

Assemblage II (samples BH134, OG589)

Coarse-grained assemblages. Garnet (<5 mm) and orthopyroxene (< 2 mm) with or without cordierite and perthite, is enveloped by S_3 biotite with or without sillimanite and rutile (Fig. 2c and d). Garnet may contain inclusions of biotite, quartz, sillimanite and rutile and also occurs as small granoblastic grains (≤1 mm). Quartz, minor sillimanite and biotite occur as inclusions in orthopyroxene, whereas smaller (≤1 mm) grains are commonly inclusion-free. Perthite and cordierite (≤1·5 mm) are part of the coarse-grained assemblage in sample BH134. The presence of cordierite and plagioclase at peak conditions for sample OG589 is uncertain.

Fine-grained assemblages. Cordierite or plagioclase may rim garnet and/or orthopyroxene (Fig. 2d). Orthopyroxene + cordierite symplectites may enclose garnet in sample OG589. Coarse-grained sillimanite is partially mantled by fine-grained sillimanite. Fine-grained biotite may occur at the margin of porphyroblastic garnet in sample BH134 (Fig. 2c).

Table 3: Si-undersaturated metapelitic mineral assemblages

Sample	SW158	SW235	SW238
sapphirine	P_7,$I_{2,3,4}$	PR_{10}	P
orthopyroxene	P	$PR_{8,12}$	P
cordierite	P?$I_3R_{5,6}$	P?R_9	P?$I_3R_{5,6}$
biotite	$PI_{1,3}R$	$PI_3R_{8,11}$	$PI_{1,3}R$
plagioclase	P?I_3R	M	M
alkali feldspar	—	M	PI_3
rutile	$PI_{1,2,3,4}$	—	—
sillimanite	—	$PR_{11,12}$	M
corundum	I_1	—	—

P, peak metamorphic assemblage; R, retrograde metamorphic assemblage; I, inclusion or prograde phase; M, minor occurrence. Subscripts: 1, inclusion in sapphirine; 2, inclusion in corundum; 3, inclusion in orthopyroxene; 4, inclusion in biotite; 5, corona to sapphirine; 6, corona to orthopyroxene; 7, corona to corundum; 8, symplectite with sillimanite; 9, symplectite with sapphirine; 10, symplectite with cordierite; 11, symplectite with orthopyroxene; 12, symplectite with biotite.

Petrography of Si-undersaturated metapelites

Coarse-grained assemblages. These samples have two domains. The first is dominated by coarse-grained sapphirine (<18 mm; Fig. 2e) and orthopyroxene (<8 mm; Fig. 2f) with or without sillimanite (<4 mm, e.g. SW235) and corundum (<8 mm, e.g. SW158). The second is biotite-rich, where biotite occurs as large poorly orientated laths (<2 mm in length) intergrown with orthopyroxene and sapphirine. Cordierite (<2·5 mm) occurs throughout the matrix, predominantly in biotite-poor domains, and embays the porphyroblastic mineral grains. Biotite, with or without sillimanite, defines an S_3 foliation that envelops pods of the two domains. Sapphirine is commonly tabular or intimately intergrown with orthopyroxene. Orthopyroxene contains sapphirine as bleb-like inclusions (Fig. 2f) or as coronae that enclose corundum inclusions (Fig. 2g). Orthopyroxene also contains inclusions

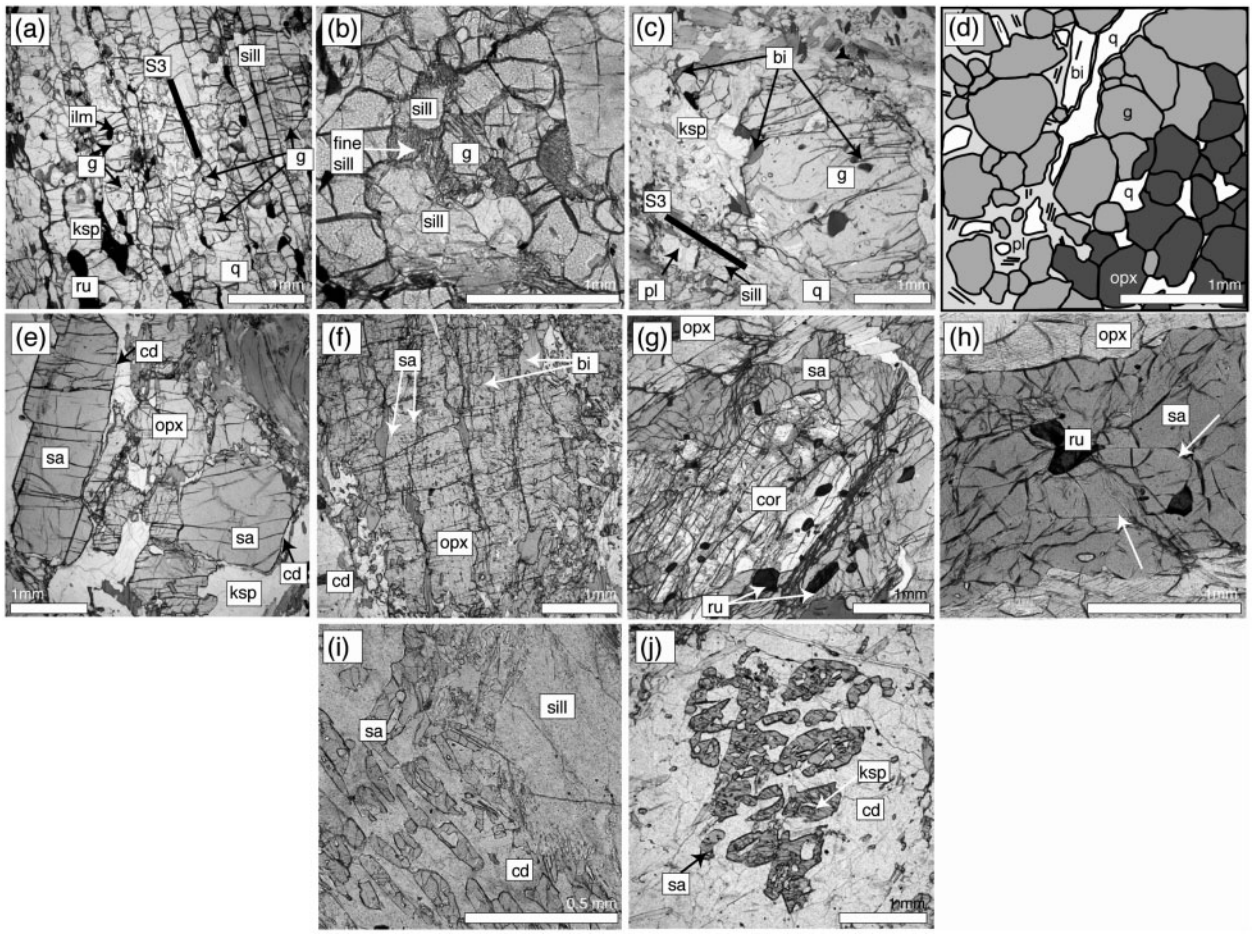

Fig. 2. Textural relationships in metapelites from Kemp Land: (a)–(d) Si-saturated metapelites; (e)–(j) Si-undersaturated metapelites. (a) Strong S_3 foliation of g + sill + ru + ksp + q in Assemblage I metapelites (SW113). Garnets may contain ilm and/or an internal sillimanite foliation commonly orientated parallel to S_3. (b) Garnet and prismatic sillimanite replaced by fine-grained sillimanite at grain boundaries in Assemblage I. (c) Porphyroblastic garnet in a lower strain orthopyroxene-absent domain of an Assemblage II metapelite (BH134). Porphyroblastic cordierite occurs nearby (not photographed). Several generations of biotite occur as inclusions, aligned in S_3 or partially pseudomorphing garnet and/or oblique to S_3. (d) Schematic sketch; orthopyroxene and garnet may be rimmed by narrow interstitial plagioclase (or cordierite) in Assemblage II (OG589). (e) Sapphirine lath (left) surrounded by a narrow corona of cordierite, which separates this mineral from orthopyroxene (SW238). (f) Orthopyroxene porphyroblast with inclusions of biotite and sapphirine blebs (SW235). (g) Sapphirine corona isolates corundum from orthopyroxene (SW158). (h) Tabular sapphirine grain (arrows show grain edge) within a sapphirine corona, probably after corundum (SW158). (i) Symplectites of sa + cd form at the edge of porphyroblastic sillimanite (SW235). (j) Sillimanite completely replaced by sa + cd symplectites. A corona of cordierite separates this reaction texture from the sillimanite- and biotite-bearing matrix (SW235).

of cordierite, biotite, rutile and plagioclase. Corundum occurs as colourless tabular to rounded grains with rutile and sapphirine inclusions; it is always enclosed by coronae of sapphirine (Fig. 2g). Locally these sapphirine coronae (0·2–2·4 mm wide) pseudomorph corundum (Fig. 2h).

Fine-grained assemblages. Symplectic intergrowths of sapphirine (sa_2) and cordierite ($cd_2 < 0{\cdot}3$ mm in width) surround coarse-grained sillimanite ($sill_1$) (Figs 2i and 3). Small blebs of alkali feldspar (ksp_2) may be present within the symplectites of sapphirine and cordierite (Figs 2j and 3). Local fine-grained symplectic intergrowths (0·01–0·1 mm) of sillimanite ($sill_2$) with or without orthopyroxene (opx_2) and biotite (bi_2) develop adjacent to the larger sillimanite grains (Fig. 3). Relict orthopyroxene (opx_1) may be observed in the vicinity of these sillimanite breakdown textures and is embayed by coronal cordierite (<1·5 mm; Fig. 3). Fine-grained sillimanite (<0·05 mm) may be developed on the rims of tabular sapphirine, which may additionally be rimmed by cordierite (<0·15 mm; Fig. 2e) or plagioclase.

Inferred parageneses

We interpret 'peak' metapelitic assemblages to consist of coarse-grained minerals that appear to have texturally equilibrated at the thin-section scale. 'Post-peak' assemblages refer to the comparatively fine-grained minerals,

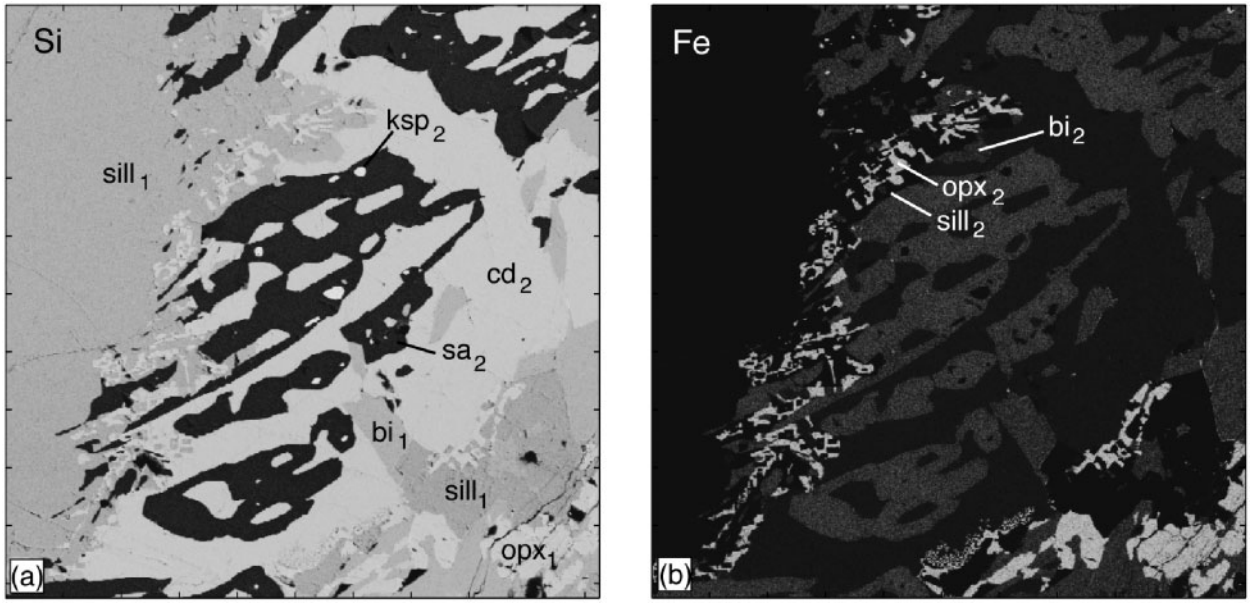

Fig. 3. Element distribution maps of (a) Si and (b) Fe showing the breakdown of porphyroblastic $sill_1$ ($+ opx_1 \pm bi_1$) to form $cd_2 + sa_2 \pm ksp_2$ symplectites in Si-undersaturated metapelite SW235. The development of fine-grained $opx_2 + sill_2 + bi_2$ at the contact with $cd_2 + sa_2 \pm ksp_2$ and $sill_1$ indicates partial replacement of the symplectic minerals.

coronal and/or symplectic textures associated with the retrograde history of the rock (Tables 2 and 3). Peak assemblages in Assemblage I metapelites are garnet, sillimanite, alkali feldspar, ilmenite, quartz with or without plagioclase, rutile, spinel and magnetite. Post-peak textures are limited but include fine-grained biotite, which rims porphyroblastic garnet or grows oblique to S_3, fine sillimanite at garnet–garnet grain boundaries and as a breakdown product of coarse sillimanite, ilmenite exsolution from biotite, and magnetite exsolution in spinel. Metapelites of Assemblage II are interpreted to locally contain peak orthopyroxene, cordierite and sillimanite, together with garnet, rutile and quartz, with or without alkali feldspar and plagioclase. Common post-peak mineral development includes narrow rims of cordierite or plagioclase around ferromagnesian minerals and fine-grained biotite and sillimanite, which replaces garnet and sillimanite.

Sapphirine is common to all Si-undersaturated metapelites from the Stillwell Hills. Distinctions in textural context and the composition (below) of sapphirine (see Tables 6 and 8; Fig. 3) allow several stages of sapphirine growth to be recognized: association I—coarse-grained coronal sapphirine enclosing corundum that is inferred to preserve part of the prograde path; association II—coarse, tabular sapphirine grains that are inferred to reflect peak conditions; association III—sapphirine + cordierite symplectites that are inferred to form during the post-peak evolution. These textures are consistent with a 'clockwise' *P–T* evolution (i.e. the thermal maximum is reached after peak pressure), as discussed below. However, Si-undersaturated, high Mg–Al metapelites are commonly chemically and mineralogically domainal at outcrop to micrometre scales; complex mineral reaction microstructures may develop primarily as a function of chemical potential rather than changing *P–T* (e.g. Hensen, 1988; Dunkley *et al.*, 1999). Therefore it can be difficult to confidently interpret the *P–T* trajectory of such rocks. If mineralogical changes are driven by changes in *P–T*, the domain-scale compositions may experience different reactions at different *P–T* conditions. The interpretation of complicated chemical and microstructural domains requires a composition-dependent approach and the consideration of chemical potential gradients.

MINERAL CHEMISTRY

The majority of chemical analyses were collected using the Cameca SX-50 Camebax electron microprobe (EMP) housed at the University of New South Wales, operating with an accelerating voltage of 15 kV and a beam current of 20 nA. Additional samples were analysed using the Macquarie University Cameca SX-100 EMP under identical operating conditions. Both sets of EMP data were reduced using the PAP data reduction software supplied by the manufacturer. Fe^{3+} was estimated on the basis of ideal stoichiometric constraints (after Droop, 1987) for garnet, orthopyroxene, spinel, sapphirine and the opaque minerals. Representative EMP analyses are presented in Tables 4–6. A summary of mineral chemistry

Table 4: Representative electron microprobe analyses for minerals from Assemblage I Si-saturated metapelites

Sample:	SW118	SW118	SW113	SW113	BH108	OG554	BH108	SW118	SW118	SW118	SW113	SW113	BH108	OG554	SW118	OG554	SW118	SW113	BH108	OG554
Mineral:	g (core)	g (rim)	g (core)	g (rim)	g (core)	g (core)	sp (g)	bi	bi (g)	bi (ksp)	bi	bi (late)	bi	bi	pl	pl	ksp	ksp	ksp	ksp
SiO_2	37·8	37·7	38·1	37·9	38·9	39·2	<0·04	37·3	36·3	35·9	37·2	37·6	37·4	37·4	58·7	63·4	64·1	63·6	64·8	64·1
TiO_2	<0·05	<0·05	<0·05	<0·05	<0·05	<0·05	<0·05	5·6	5·0	6·0	5·0	4·9	5·1	4·9	<0·05	<0·05	<0·05	<0·05	<0·05	<0·05
Al_2O_3	21·9	21·7	21·7	21·5	21·9	22·5	59·7	15·9	15·1	15·2	15·0	14·5	15·6	14·8	26·0	23·0	18·8	19·0	18·7	18·8
Cr_2O_3	0·1	<0·07	<0·07	<0·07	<0·07	<0·07	0·4	0·1	<0·07	0·1	0·1	<0·07	<0·07	0·2	<0·07	<0·07	<0·07	<0·07	<0·07	<0·07
Fe_2O_3	2·3	2·3	1·3	2·3	1·7	1·1	4·4	—	—	—	—	—	—	—	—	—	—	—	—	—
FeO	27·0	27·1	27·3	27·3	26·1	25·0	18·2	10·1	11·1	12·8	10·4	9·4	11·6	9·6	<0·08	<0·08	<0·08	<0·08	<0·08	<0·08
MnO	0·5	0·4	1·0	1·2	0·6	0·3	<0·06	<0·06	<0·06	<0·06	<0·06	<0·06	<0·06	<0·06	<0·06	<0·06	<0·06	<0·06	<0·06	<0·06
MgO	8·9	8·9	8·9	8·7	10·2	11·2	10·0	16·6	17·0	14·3	17·1	18·2	16·2	16·7	<0·06	<0·06	<0·06	<0·06	<0·06	<0·06
CaO	1·4	1·4	0·9	1·0	1·4	1·1	<0·04	<0·04	<0·04	<0·04	<0·04	<0·04	<0·04	<0·04	7·6	3·8	0·1	<0·04	0·1	0·2
Na_2O	<0·04	<0·04	<0·04	<0·04	<0·04	<0·04	0·2	0·1	0·1	0·2	0·2	0·1	0·1	0·3	7·0	8·9	1·5	1·6	2·0	2·5
K_2O	<0·03	<0·03	<0·03	<0·03	<0·03	<0·03	<0·03	9·7	9·4	10·1	9·6	9·7	10·1	9·8	0·2	0·6	14·4	14·0	14·0	13·1
ZnO	n.a.	n.a.	n.a.	n.a.	n.a.	n.a.	7·2	n.a.	n.a.	n.a.	n.a.	n.a.	n.a.	n.a.	n.a.	n.a.	n.a.	n.a.	n.a.	n.a.
Total	99·9	99·5	99·4	99·9	100·7	100·5	100·2	95·3	93·9	94·5	94·6	94·4	96·1	93·6	99·5	99·7	98·9	98·3	99·5	98·8
Si	2·93	2·94	2·97	2·95	2·97	2·96	—	5·44	5·42	5·39	5·49	5·53	5·47	5·56	2·63	2·81	2·98	2·97	2·99	2·97
Ti	—	—	—	—	—	—	—	0·61	0·56	0·67	0·56	0·54	0·56	0·55	—	—	—	—	—	—
Al	2·00	1·99	1·99	1·97	1·97	2·01	1·91	2·73	2·65	2·69	2·61	2·52	2·69	2·59	1·37	1·20	1·03	1·05	1·01	1·03
Cr	0·01	—	—	—	—	—	0·01	0·01	—	0·01	0·01	—	—	0·02	—	—	—	—	—	—
Fe^{3+}	0·13	0·13	0·08	0·13	0·10	0·07	0·09	—	—	—	—	—	—	—	—	—	—	—	—	—
Fe	1·75	1·76	1·78	1·77	1·67	1·58	0·41	1·23	1·39	1·61	1·28	1·16	1·42	1·19	—	—	—	—	—	—
Mn	0·03	0·03	0·07	0·08	0·04	0·02	—	—	—	—	—	—	—	—	—	—	—	—	—	—
Mg	1·03	1·03	1·04	1·01	1·16	1·26	0·41	3·62	3·77	3·20	3·76	3·99	3·53	3·70	—	—	—	—	—	—
Ca	0·12	0·12	0·08	0·08	0·11	0·09	—	—	—	—	—	—	—	—	0·37	0·18	—	—	—	0·01
Na	—	—	—	—	—	—	0·01	0·03	0·03	0·05	0·04	0·04	0·03	0·08	0·61	0·77	0·14	0·14	0·18	0·23
K	—	—	—	—	—	—	—	1·81	1·79	1·94	1·82	1·83	1·88	1·86	0·01	0·03	0·85	0·83	0·82	0·78
Zn	n.a.	n.a.	n.a.	n.a.	n.a.	n.a.	0·16	n.a.	n.a.	n.a.	n.a.	n.a.	n.a.	n.a.	n.a.	n.a.	n.a.	n.a.	n.a.	n.a.
Total	8·00	8·00	8·00	8·00	8·00	8·00	3·00	15·49	15·61	15·58	15·57	15·61	15·59	15·55	4·99	4·99	5·00	5·00	5·01	5·02
X_{Mg}	0·35	0·35	0·36	0·35	0·40	0·43	0·45	0·75	0·73	0·67	0·75	0·78	0·71	0·76	—	—	—	—	—	—
X_{Mg}*	0·37	0·37	0·37	0·36	0·41	0·44	0·50	—	—	—	—	—	—	—	—	—	—	—	—	—

Mineral in parentheses indicates host to inclusion; —, variable has not been calculated; n.a., not analysed. Lower limits of detection values are based on theoretical counting statistics for 10 s count times.
*Excluding Fe^{3+}.

Table 5: Representative electron microprobe analyses for minerals from Assemblage II Si-saturated metapelites

Sample:	BH134	BH134	OG589	OG589	OG589	BH134	BH134	OG589	BH134	BH134	OG589	BH134	OG589	BH134
Mineral:	g (core)	g (rim)	g (core)	opx (core)	opx (rim)	cd (core)	cd (rim)	crd (rim)	bi	bi (g)	bi	pl	pl	ksp
SiO_2	38·4	38·3	40·6	50·9	51·6	49·7	48·8	49·1	36·7	37·0	37·8	60·2	62·1	63·9
TiO_2	<0·05	<0·05	<0·05	0·1	0·1	<0·05	<0·05	<0·05	5·7	5·4	4·7	<0·05	<0·05	0·1
Al_2O_3	22·4	22·1	23·6	8·4	7·7	33·6	33·4	33·8	14·7	15·3	14·8	24·7	23·7	18·4
Cr_2O_3	0·1	0·2	0·1	0·1	0·1	<0·07	<0·07	<0·07	0·3	0·5	0·3	<0·07	<0·07	<0·07
Fe_2O_3	2·2	2·5	1·1	0·9	0·7	—	—	—	—	—	—	—	—	—
FeO	24·2	24·6	17·2	11·1	11·1	3·1	3·1	1·7	11·2	8·9	7·0	<0·08	<0·08	<0·08
MnO	0·2	0·2	0·2	0·1	<0·06	<0·06	<0·06	<0·06	<0·06	<0·06	<0·06	<0·06	<0·06	<0·06
MgO	11·4	11·0	16·8	27·8	28·3	11·7	11·6	12·6	15·7	16·8	19·5	<0·06	<0·06	<0·06
CaO	1·0	1·1	0·7	<0·04	<0·04	<0·04	<0·04	<0·04	<0·04	<0·04	<0·04	6·5	4·6	0·1
Na_2O	<0·04	<0·04	<0·04	<0·04	<0·04	<0·04	<0·04	0·1	0·1	0·2	0·2	7·3	8·8	1·4
K_2O	<0·03	<0·03	<0·03	<0·03	<0·03	<0·03	<0·03	<0·03	9·9	9·9	9·7	0·3	0·2	14·6
Total	99·9	99·9	100·3	99·4	99·7	98·2	97·2	97·3	94·5	94·1	93·8	98·9	99·6	98·5
Si	2·93	2·93	2·96	1·81	1·83	5·00	4·97	4·95	5·47	5·47	5·53	2·70	2·76	2·98
Ti	—	—	—	—	—	—	—	—	0·64	0·60	0·51	—	—	—
Al	2·01	1·99	2·03	0·35	0·32	3·99	4·01	4·02	2·58	2·66	2·55	1·30	1·24	1·01
Cr	0·01	0·01	—	—	—	—	—	—	0·04	0·05	0·03	—	—	—
Fe^{3+}	0·12	0·14	0·06	0·02	0·02	—	—	—	—	—	—	—	—	—
Fe	1·54	1·57	1·05	0·33	0·33	0·26	0·27	0·15	1·40	1·10	0·85	—	—	—
Mn	0·01	0·01	0·01	—	—	—	—	—	—	—	—	—	—	—
Mg	1·29	1·26	1·83	1·48	1·49	1·75	1·76	1·90	3·48	3·70	4·25	—	—	—
Ca	0·08	0·09	0·06	—	—	—	—	—	—	—	—	0·31	0·22	—
Na	—	—	—	—	—	—	—	0·01	0·03	0·07	0·06	0·64	0·76	0·13
K	—	—	—	—	—	—	—	—	1·89	1·86	1·81	0·01	0·01	0·87
Total	8·00	8·00	8·00	4·00	4·00	11·00	11·02	11·04	15·54	15·52	15·60	4·97	5·00	5·00
X_{Mg}	0·44	0·42	0·62	0·81	0·81	—	—	—	—	—	—	—	—	—
X_{Mg}*	0·46	0·44	0·64	0·82	0·82	0·87	0·87	0·93	0·71	0·77	0·83	—	—	—

Mineral in parentheses indicates host to inclusion; —, variable has not been calculated. Lower limits of detection values are based on theoretical counting statistics for 10 s count times
*Excluding Fe^{3+}.

for the samples used in pseudosection calculations is given below and summarized in Tables 7 and 8.

Si-saturated metapelites

Assemblage I garnet is an almandine-rich, almandine–pyrope solid solution with $X_{Alm} = Fe^{total}/(Fe^{total} + Mn + Mg + Ca) = 0{\cdot}54–0{\cdot}64$ and $X_{Pyp} = Mg/(Fe^{total} + Mn + Mg + Ca) = 0{\cdot}31–0{\cdot}43$ with minor $X_{Gross} = Ca/(Fe^{total} + Mn + Mg + Ca) \leq 0{\cdot}04$ and $X_{Spess} = Mn/(Fe^{total} + Mn + Mg + Ca) \leq 0{\cdot}03$ for most samples (Tables 4, 5 and 7). Garnet in Assemblage II is a pyrope–almandine solid solution with $X_{Pyp} = 0{\cdot}40–0{\cdot}63$ and $X_{Alm} = 0{\cdot}35–0{\cdot}57$. Garnet may have a subtle rimward enrichment in Fe, and a decrease in Mg and Ca; the variation is limited and there are no systematic differences in the composition of garnet orientated in the foliation compared with porphyroblastic garnet.

Assemblage I biotite inclusions in garnet [$X_{Mg} = Mg/(Fe + Mg) = 0{\cdot}73–0{\cdot}74$] are more magnesian than inclusions in alkali feldspar ($X_{Mg} = 0{\cdot}65–0{\cdot}67$). Matrix biotite in Assemblage I includes biotite in the S_3 foliation ($X_{Mg} = 0{\cdot}69–0{\cdot}77$), and subtly more magnesian post-S_3 biotite ($X_{Mg} = 0{\cdot}75–0{\cdot}78$). Assemblage I biotite contains 0·54–0·67 Ti cations per formula unit (p.f.u.) based on 22 oxygen. Biotite in Assemblage II has $X_{Mg} = 0{\cdot}69–0{\cdot}86$ and Ti content of 0·44–0·73 p.f.u. The range in compositions within each sample is restricted to variation in $X_{Mg} < 0{\cdot}08$ (Table 7).

Table 6: Representative electron microprobe analyses for minerals from Si-undersaturated metapelites

Sample:	SW158	SW158	SW235	SW238	SW238	SW158	SW235	SW235	SW238	SW238	SW158	SW238	SW235	SW235	SW158	SW238	SW235	SW158	SW238	SW238
Mineral:	sa1 (cor)	sa1 (opx)	sa2	sa1 (core)	sa1 (rim)	opx1	opx1 (core)	opx2	opx1 (core)	opx1 (rim)	bi	bi	bi	bi2	cd	cd2	cd2	pl	pl	ksp
SiO_2	12·4	12·7	13·2	13·4	12·8	51·8	50·7	51·7	49·7	50·4	37·5	38·2	38·7	39·7	49·6	49·8	49·3	55·0	67·5	63·9
TiO_2	0·1	<0·05	<0·05	0·1	<0·05	<0·05	0·1	<0·05	<0·05	0·1	3·4	2·6	0·7	0·2	<0·05	<0·05	<0·05	<0·05	<0·05	<0·05
Al_2O_3	62·9	62·4	63·1	62·0	63·8	7·3	8·5	6·1	8·9	8·4	16·0	16·6	16·1	17·1	33·9	34·4	34·4	28·3	19·7	18·5
Cr_2O_3	0·1	0·2	<0·07	<0·07	<0·07	<0·07	<0·07	<0·07	<0·07	<0·07	<0·07	0·1	<0·07	<0·07	<0·07	<0·07	0·1	<0·07	<0·07	<0·07
Fe_2O_3	3·8	3·1	1·0	1·3	1·1	2·4	0·4	0·8	1·3	1·3	—	—	—	—	—	—	—	—	—	—
FeO	1·9	2·2	5·6	5·1	5·2	7·8	13·8	14·6	13·2	13·1	5·6	6·8	5·7	5·1	1·3	2·3	2·4	0·1	0·1	0·1
MnO	0·1	0·1	<0·06	0·1	0·1	0·2	0·2	0·3	0·2	0·3	<0·06	<0·06	<0·06	<0·06	<0·06	<0·06	<0·06	0·1	0·1	<0·06
MgO	18·4	18·4	17·0	17·3	17·0	30·3	26·1	26·2	25·8	26·3	20·7	19·9	21·7	22·4	13·1	12·2	12·2	<0·06	<0·06	<0·06
CaO	<0·04	0·1	<0·04	<0·04	<0·04	<0·04	0·1	<0·04	<0·04	<0·04	<0·04	<0·04	<0·04	<0·04	<0·04	<0·04	<0·04	10·3	0·1	<0·04
Na_2O	0·1	0·1	<0·04	<0·04	<0·04	<0·04	<0·04	<0·04	<0·04	<0·04	0·4	0·2	0·2	0·3	<0·04	0·1	<0·04	5·5	11·6	1·3
K_2O	<0·03	<0·03	<0·03	<0·03	<0·03	<0·03	<0·03	<0·03	<0·03	<0·03	9·6	10·0	9·7	10·0	<0·03	<0·03	<0·03	0·1	0·1	14·6
Total	99·8	99·3	100·0	99·4	100·0	99·8	100·0	99·8	99·2	99·9	93·3	94·3	92·9	94·9	98·0	98·8	98·5	99·4	99·0	98·5
Si	1·46	1·51	1·56	1·59	1·51	1·82	1·81	1·86	1·79	1·80	5·48	5·55	5·66	5·66	4·96	4·96	4·93	2·49	2·98	2·98
Ti	0·01	—	—	0·01	—	—	—	—	—	—	0·37	0·29	0·07	0·02	—	—	—	—	—	—
Al	8·74	8·71	8·79	8·69	8·87	0·30	0·36	0·26	0·38	0·36	2·76	2·84	2·78	2·88	4·00	4·04	4·07	1·51	1·02	1·02
Cr	0·01	0·02	—	—	—	—	—	—	—	—	—	0·01	—	—	—	—	—	—	—	—
Fe^{3+}	0·33	0·28	0·09	0·12	0·10	0·06	0·01	0·02	0·03	0·04	—	—	—	—	—	—	—	—	—	—
Fe	0·19	0·21	0·55	0·51	0·51	0·23	0·41	0·44	0·40	0·39	0·69	0·83	0·70	0·61	0·11	0·19	0·20	0·01	—	—
Mn	0·01	0·01	—	0·01	0·01	0·01	0·01	0·01	0·01	0·01	—	—	—	—	—	—	—	—	—	—
Mg	3·24	3·24	2·99	3·08	2·99	1·58	1·39	1·41	1·39	1·40	4·50	4·29	4·73	4·77	1·95	1·82	1·82	—	—	—
Ca	—	0·01	—	—	—	—	—	—	—	—	—	—	—	—	—	—	—	0·50	—	—
Na	0·01	0·01	—	—	—	—	—	—	—	—	0·13	0·04	0·05	0·08	0·01	0·01	0·01	0·48	0·99	0·12
K	—	—	—	—	—	—	—	—	—	—	1·79	1·85	1·82	1·82	—	—	—	0·01	—	0·87
Total	14·00	14·00	14·00	14·00	14·00	4·00	4·00	4·00	4·00	4·00	15·72	15·69	15·81	15·83	11·04	11·03	11·04	5·00	5·01	5·00
y(mineral)	0·28	0·28	0·37	0·31	0·41	0·13	0·17	0·12	0·18	0·16	—	—	—	—	—	—	—	—	—	—
y(mineral)*	0·19	0·21	0·35	0·28	0·39	0·12	0·17	0·12	0·17	0·16	—	—	—	—	—	—	—	—	—	—
X_{Mg}	0·86	0·87	0·82	0·83	0·83	0·84	0·77	0·75	0·76	0·77	—	—	—	—	—	—	—	—	—	—
X_{Mg}*	0·94	0·94	0·84	0·86	0·85	0·87	0·77	0·76	0·78	0·78	0·87	0·84	0·87	0·89	0·95	0·90	0·90	—	—	—

Mineral in parentheses indicates host to inclusion; —, variable has not been calculated. Lower limits of detection values are based on theoretical counting statistics for 10 s count times.
*Excluding Fe^{3+}.

Table 7: Summary of mineral chemistry of Si-saturated metapelites

	Assemblage I (Fe-rich)				Assemblage II (Mg-rich)	
Sample:	SW113	SW118	BH108	OG554	BH134	OG589
X_{Mg} (bulk)	0·32	0·36	0·35	0·43	0·59	0·70
X_{Mg} (g)	0·32–0·36	0·33–0·36	0·36–0·40	0·42–0·44	0·41–0·46	0·60–0·64
X_{Mg}* (g)	0·34–0·38	0·35–0·37	0·37–0·41	0·43–0·45	0·42–0·47	0·62–0·97
X_{Mg} (opx)	n.p.	n.p.	n.p.	n.p.	n.a.	0·80–0·82
X_{Mg}* (opx)	n.p.	n.p.	n.p.	n.p.	n.a.	0·82–0·83
X_{Mg} (cd)	n.p.	n.p.	n.p.	n.p.	0·86–0·88	0·92–0·93
X_{Mg} (bi)	0·74–0·78	0·65–0·75	0·69–0·73	0·75–0·77	0·69–0·77	0·83–0·86
Ti p.f.u. (bi)	0·54–0·57	0·56–0·67	0·55–0·60	0·55–0·60	0·44–0·76	0·44–0·56
X_{An} (pl)	n.p.	0·33–0·39	n.a.	0·18–0·19	0·32–0·34	0·22–0·26
X_{Or} (ksp)	0·79–0·86	0·84–0·90	0·82–0·89	0·77–0·90	0·80–0·89	n.p.
X_{Ab} (ksp)	0·13–0·20	0·10–0·15	0·11–0·18	0·09–0·23	0·11–0·19	n.p.
X_{An} (ksp)	≤0·02	≤0·01	≤0·01	≤0·01	≤0·01	n.p.
X_{herc} (sp)	n.p.	n.p.	0·36–0·38	n.p.	n.p.	n.p.
X_{Spl} (sp)	n.p.	n.p.	0·42	n.p.	n.p.	n.p.
X_{gah} (sp)	n.p.	n.p.	0·16–0·18	n.p.	n.p.	n.p.
X_{Mt} (sp)	n.p.	n.p.	0·04	n.p.	n.p.	n.p.
X_{Hem} (ilm)	0·02	≤0·02	0·04–0·14	n.p.	n.p.	n.p.

*Excluding Fe^{3+}.
n.p., not present; n.a., present, not analysed.

Table 8: Summary of mineral chemistry of Si-undersaturated metapelites

Sample:	SW158	SW235	SW238
X_{Mg} (bulk)	0·87	0·84	0·81
X_{Mg} (sa)	0·85–0·88	0·82–0·85	0·82–0·84
X_{Mg}* (sa)	0·90–0·94	0·82–0·86	0·84–0·87
y(sa)	0·21–0·46	0·27–0·48	0·27–0·47
y(sa)*	0·14–0·41	0·23–0·47	0·24–0·44
X_{Mg} (opx)	0·84–0·85	0·74–0·78	0·75–0·77
X_{Mg}* (opx)	0·83–0·89	0·74–0·78	0·76–0·79
y(opx)	0·13–0·18	0·12–0·19	0·12–0·20
y(opx)*	0·12–0·18	0·12–0·19	0·12–0·19
X_{Mg} (crd)	0·94–0·95	0·89–0·91	0·89–0·91
X_{Mg} (bi)	0·87–0·88	0·86–0·89	0·84–0·87
Ti p.f.u. (bi)	0·30–0·37	0·01–0·11	0·02–0·29
X_{An} (pl)	0·44–0·51	n.p.	0·99
X_{Or} (ksp)	n.p.	0·88–0·89	0·67–0·88
X_{Ab} (ksp)	n.p.	0·11–0·12	0·12–0·32
X_{An} (ksp)	n.p.	<0·01	≤0·01

*Excluding Fe^{3+}.
n.p., not present.

Biotite inclusions in garnet (e.g. BH134; $X_{Mg} = 0{\cdot}74–0{\cdot}77$) are commonly more magnesian than matrix biotite ($X_{Mg} = 0{\cdot}69–0{\cdot}74$).

Spinel (Assemblage I) has end-member compositions of $X_{Herc} = (Fe^{2+} - Fe^{Mt})/(Fe^{2+} + Mg + Zn) = 0{\cdot}36–0{\cdot}38$, where Fe^{Mt} is the amount of Fe^{2+} devoted to magnetite, $X_{Spl} = Mg/(Fe^{2+} + Mg + Zn) = 0{\cdot}42$, $X_{Gah} = Zn/(Fe^{2+} + Mg + Zn) = 0{\cdot}16–0{\cdot}18$ and $X_{Mt} = Fe^{Mt}/(Fe^{2+} + Mg + Zn) = 0{\cdot}04$ (Table 7). Ilmenite ranges between a pure end-member composition and an ilmenite–hematite solid solution with $X_{Hem} = 0{\cdot}02–0{\cdot}14$.

Cordierite (Assemblage II) has $X_{Mg} = Mg/(Fe^{total} + Mg) = 0{\cdot}86–0{\cdot}93$ (Table 6). Individual cordierite grains are not zoned. Orthopyroxene (Assemblage II) varies in the range $X_{Mg} = Mg/(Fe^{total} + Mg) = 0{\cdot}80–0{\cdot}82$ (Table 7). Al content ranges from 0·23 to 0·35 p.f.u. with no apparent zoning. Alkali feldspar is commonly microperthitic with $X_{Or} = K/(Ca + Na + K) = 0{\cdot}77–0{\cdot}90$ (Table 7). Plagioclase varies in the range $X_{An} = Ca/(Ca + Na) = 0{\cdot}18–0{\cdot}39$ (Table 7). Sillimanite contains less than 0·5 wt % Fe_2O_3 (analysed as FeO) in most samples, but up to 1·3 wt % Fe_2O_3 in sample BH108. Rutile contains up to 0·2 wt % Fe_2O_3 (analysed as FeO).

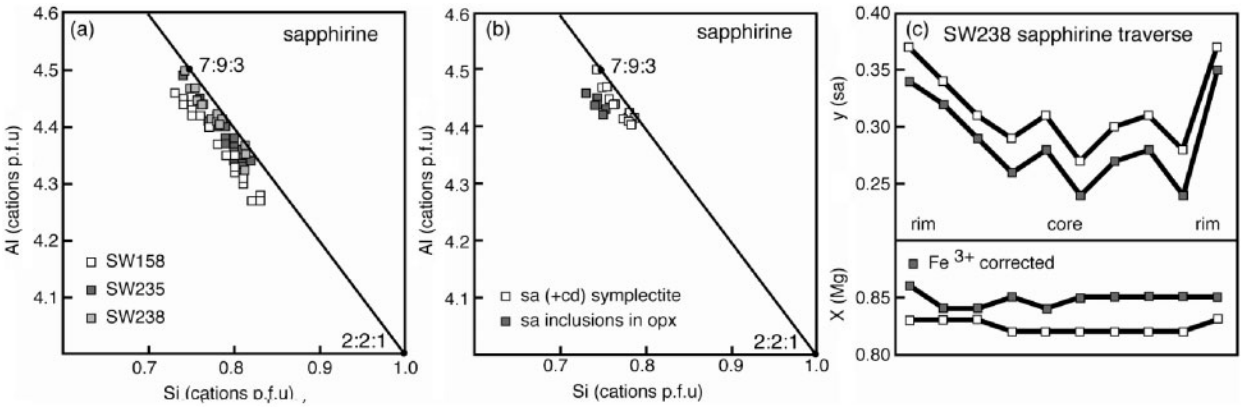

Fig. 4. Compositional variation of sapphirine from Si-undersaturated metapelites from the Stillwell Hills. (a) Al vs Si for three samples. The spread to lower-Al, higher-Si compositions is from coronal sapphirine and/or porphyroblast analyses. (b) Al vs Si for sapphirine (+cd) symplectites and sapphirine inclusions in orthopyroxene cluster close to the 7:9:3 stoichiometric composition line. (c) A zoning profile in y(sa) from core to rim may be marked in large sapphirine porphyroblasts (e.g. sample SW238), whereas X_{Mg} shows little variation.

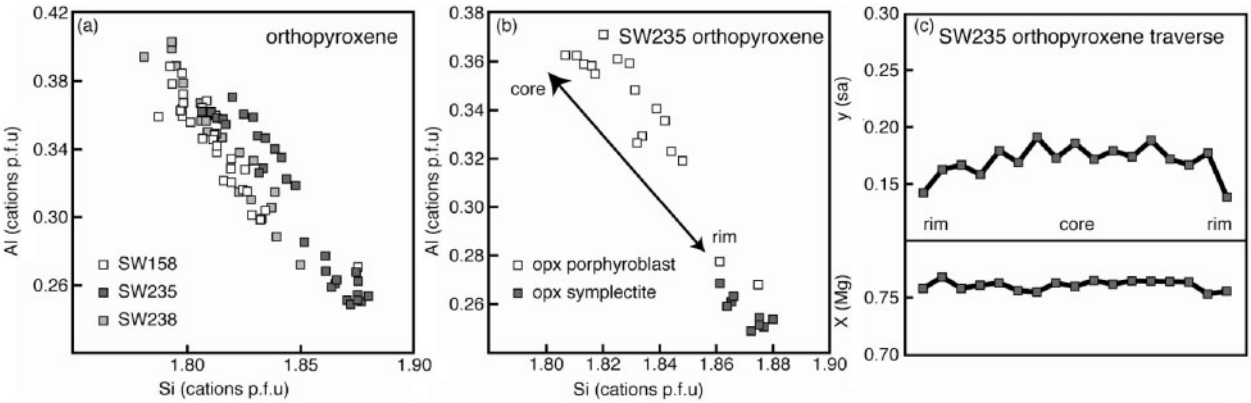

Fig. 5. Compositional variation of orthopyroxene from Si-undersaturated metapelites from the Stillwell Hills. (a) Al vs Si for three samples. The analyses with the highest Si and lowest Al are mostly obtained from symplectites in sample SW235 (Fig. 5b). (b) Al vs Si for an orthopyroxene porphyroblast in sample SW235 (shown in Fig. 2f). Rim compositions trend towards symplectic orthopyroxene compositions for the same rock. (c) A zoning profile in y(opx) across the orthopyroxene porphyroblast from (b) shows the opposite trend to y(sa) (Fig. 4c). The X_{Mg} trend is relatively flat.

Si-undersaturated metapelites

Sapphirine composition varies considerably with textural context with $X_{Mg} = 0{\cdot}82$–$0{\cdot}88$ and the Al content, or $y(\text{sa}) \equiv X^{M1}{}_{Al}$, ranges from 0·19 to 0·48 (Table 8). Figure 4 shows Al vs Si for sapphirine analyses, all of which lie below the ideal Tschermak's substitution line between (Mg:Al:Si) compositions 2:2:1 and 7:9:3 (Fig. 4a and b) implying considerable incorporation of Fe^{3+} in some cases (Tables 6 and 8). Compositions cluster closer to the 7:9:3 stoichiometric ratio (where Al = 4·5, Si = 0·75 p.f.u. on the basis of 10 oxygen). Sapphirine blebs in large orthopyroxene grains show compositions close to symplectic sapphirine; however, they are more enriched in Fe^{3+} (Fig. 4b). A large compositional range in coronal sapphirine reflects the position within the corona and/or proximity to neighbouring minerals; inner coronal sapphirine against corundum is richest in Al and is Si-poor. The majority of coarse-grained porphyroblastic sapphirines are Si-rich and Al-poor compared with finer-grained symplectic sapphirine (Fig. 4a and b). The cores of porphyroblastic sapphirine have higher Si and lower Al than rim compositions, resulting in marked y(sa) profiles, with comparatively little variation in X_{Mg} across the grain (Fig. 4c).

Orthopyroxene compositions (Fig. 5) vary in the range $X_{Mg} = 0{\cdot}84$–$0{\cdot}85$ for corundum-bearing sample SW158 and $X_{Mg} = 0{\cdot}74$–$0{\cdot}78$ for samples SW235 and SW238 (Table 8). Zoning in Al content is apparent with $y(\text{opx}) \equiv X^{M1}{}_{Al} = 0{\cdot}12$–$0{\cdot}20$ (Table 8). Porphyroblast rim compositions have higher Si and lower Al than cores [$y(\text{opx})_{rim} < y(\text{opx})_{core}$] and trend towards Si-rich/Al-poor

symplectic orthopyroxene (Fig. 5b and c). This relationship is the opposite of that observed for sapphirine compositions. Variation in X_{Mg} (opx) across orthopyroxene porphyroblasts is minimal (Fig. 5c).

Biotite is highly magnesian, reflecting the bulk-rock compositions (Table 8). Biotite inclusions in cordierite, sapphirine and orthopyroxene have slightly lower X_{Mg} (bi) ($\leq$0·02) than biotite in the matrix. Ti content varies between samples, presumably as a result of rock composition; sample SW158 has higher Ti (0·30–0·37 p.f.u.) than samples SW235 and SW238 (0·01–0·29 p.f.u.). Fine-grained biotite involved in symplectite textures in SW235 has the lowest Ti values (0·01–0·02 p.f.u.), similar to the range of late biotite on the edge of orthopyroxene ± cordierite in SW238 (0·02–0·09 p.f.u.).

Cordierite shows a restricted range of compositions between samples (X_{Mg} = 0·89–0·95), which is further restricted ($\leq$0·02) within individual samples (Table 8). Alkali feldspar in the matrix in SW238 has X_{Or} = 0·67–0·88. Small blebs of alkali feldspar intergrown with symplectic sapphirine in SW235 have X_{Or} = 0·88–0·89 (Table 8). Inclusions of plagioclase in orthopyroxene have higher X_{An} values (0·50–0·51) than matrix plagioclase (0·44–0·45) in SW158. Rare plagioclase in SW238 rims sapphirine porphyroblasts and is close to pure anorthite (Table 8). Sillimanite contains up to 0·4 wt % Fe_2O_3, rutile contains up to 1·4 wt % Fe_2O_3 and corundum up to 0·7 wt % Fe_2O_3 (all analysed as FeO) and 0·2 wt % Cr_2O_3.

P–T METAMORPHIC CONDITIONS

Methodology of *P–T* pseudosection calculations

To constrain the peak and retrograde history of the metapelites from Kemp Land, a series of *P–T* pseudosections relevant to the mineral assemblages preserved in these rocks are presented in the following section. Pseudosections are more useful for interpreting mineral textures than petrogenetic *P–T* grids as they portray and quantify multivariant equilibria. Mineral assemblage fields are contoured for mineral proportions, providing additional constraints on the interpretation of metamorphic microstructures.

The pseudosections presented in this study for the Si-saturated metapelites were calculated in the NCKFMASHTO chemical system using the software THERMOCALC v3.25 (Powell & Holland, 1988) and the internally consistent dataset of Holland & Powell (1998, updated 22 November 2003). The omission of MnO from the calculations is likely to overestimate the temperature at which garnet becomes stable by a small amount. New mixing models for garnet, biotite and liquid (silicate melt), have been utilized in this NCKFMASHTO system (White *et al.*, 2007). The *a–x* relationships for orthopyroxene, spinel and magnetite are taken from White *et al.* (2002), ilmenite from White *et al.* (2000), osumilite from Holland *et al.* (1996) and the remaining minerals are those used by White *et al.* (2001). This model system incorporates TiO_2 and Fe_2O_3 (White *et al.*, 2002), which have been shown to affect the stability of biotite and spinel at high temperatures (e.g. Indares & Martignole, 1985; Sack & Ghiorso, 1991; Kleeman & Reinhardt, 1996). These components also allow the consideration of rutile and ilmenite, both minerals occurring within the peak assemblages in the Si-saturated metapelites in Kemp Land. *P–T* pseudosections for the Si-undersaturated metapelites are calculated in the NCKFMASH chemical system, as there is currently no *a–x* model for Fe^{3+}-bearing sapphirine. The *a–x* relationships for sapphirine are those of Kelsey *et al.* (2004, 2005). NCKFMASH calculations here use the mineral and melt *a–x* relationships and non-ideal parameters of White *et al.* (2001).

A critical consideration in the calculation of these pseudosections is the estimation of an appropriate bulk chemical composition, which must take into account the equilibration volume of the mineral assemblage observed in thin section. In rocks with considerable mineral zoning it may be necessary to exclude certain areas for the effective bulk composition, such as the cores of porphyroblastic minerals (e.g. Marmo *et al.*, 2002). For medium- to high-grade rocks, a representative bulk composition is commonly estimated using molecular proportions recalculated from X-ray fluorescence (XRF) analyses (e.g. Kelsey *et al.*, 2005). This method may be applied if the rocks are relatively homogeneous and minerals largely unzoned. In this study, representative bulk compositions of the Assemblage I Si-saturated samples were estimated by XRF from cuts of the hand specimen that was used for thin-section preparation. Metapelites of Assemblage II are domainal with respect to the distribution of ferromagnesian minerals (and sillimanite in OG589). Although XRF analyses were used for peak *P–T* calculations for these Assemblage II rocks, a number of fields in the pseudosections appropriate to these domains are included as representative of the peak mineral assemblage. This will be discussed in further detail below. *P–T* pseudosections for Si-undersaturated metapelites were calculated with a bulk composition derived from XRF analyses where the samples are relatively coarse-grained (e.g. SW158, SW238). To model finer-grained, post-peak microstructures in sample SW235 an element map of a selected area of the thin section (Fig. 3) allowed for a bulk composition calculation after a matrix correction (after Clarke *et al.*, 2001). The amount of H_2O used for *P–T* pseudosection calculations was approximated by the 'loss on ignition' (LOI) value in the bulk analysis. An estimation of Fe_2O_3

Table 9: Bulk compositions used for P–T *pseudosection calculations (in molar oxide per cent)*

Sample	Fig. no.	H_2O	SiO_2	Al_2O_3	CaO	MgO	FeO	K_2O	Na_2O	TiO_2	O
SW118	6a	1·09	77·92	8·41	0·93	2·88	5·05	1·89	1·22	0·57	0·04
SW113	6b	1·66	63·51	15·07	0·39	4·57	9·92	2·84	1·16	0·83	0·04
BH108	6c	1·74	54·4	16·72	0·57	7·77	14·24	1·69	0·35	1·25	1·26
BH134	6d	1·79	59·62	14·39	1·21	10·86	7·65	1·98	1·63	0·81	0·06
OG554	6e	1·54	65·38	12·2	0·71	6·75	8·86	2·71	1·16	0·64	0·05
OG589	6f	0·75	51·66	10·7	0·67	24·35	10·79	0·32	0·5	0·22	0·05
SW158	8a	2·29	42·03	13·03	0·21	34·5	5·14	1·53	0·38	—	—
SW238	8b	1·45	43·34	16·7	0·03	29·06	6·97	2·01	0·44	—	—
SW235	8c	2·6	45·46	30·31	0·29	16·72	3·27	1·04	0·31	—	—

(which is recast as 'O' in the NCKFMASHTO system, Table 9) was based on the abundance of the Fe^{3+}-bearing minerals and modal constraints in the context of recalculated EMP analyses. In most cases the estimated amount of Fe^{3+} is low because of the paucity of minerals in the assemblage known to contain considerable Fe^{3+} (e.g. oxide minerals). Garnet and/or orthopyroxene in the analysed rocks have little Fe^{3+} (Tables 4, 5 and 7). In Fe-rich Assemblage I rocks, Fe^{3+}-bearing minerals are somewhat more common, particularly in the case of the sample selected from Broka and Havstein Islands (BH108). The effect of altering the estimated Fe_2O_3 is discussed below.

P–T constraints from Si-saturated metapelites

Two Si-saturated metapelites from each of the three locations were chosen for the calculation of *P–T* pseudosections. Where possible, bulk-rock compositions at each location (Table 9) were chosen to provide a marked contrast in X_{Mg} (bulk; Table 7).

Estimation of peak conditions

The (inferred) peak metamorphic assemblages for the Si-saturated metapelites from the Kemp Land coast (Table 2) correspond to assemblage fields (in bold outline) in the pseudosections in Fig. 6a–f. As samples chosen for this study come from a small area at each location, the groupings are interpreted to have shared metamorphic histories and to have experienced similar peak *P–T* conditions (i.e. local field gradients, if present, were insignificant). The two bulk compositions from each location can therefore be used to constrain the peak *P–T* conditions for the area. This technique involves 'overlapping' the peak assemblage fields for the two samples (hatched areas in Fig. 6); the region of *P–T* space shared by these compositions may be considered as the peak *P–T* conditions for the area (Kelsey *et al.*, 2003*c*). In the case of Assemblage II metapelites, several fields may be interpreted as peak assemblages, appropriate to different local textural domains. In all samples modelled, the inferred stability of biotite is pivotal to the interpretation of a lower limit to peak conditions. Biotite is excluded from the interpreted peak assemblage fields below because the petrographic observations are ambiguous and the NCKFMASHTO model system lacks F and Cl, and thus probably underestimates biotite stability (Peterson *et al.*, 1991; Nair & Chacko, 2002).

The hatched areas on *P–T* pseudosections in Fig. 6 show the overlapping *P–T* space for peak metapelitic assemblages from the Stillwell Hills, Broka and Havstein Islands and the Oygarden Group. Overlapping peak assemblages for the Stillwell Hills (Fig. 6a and b) are the garnet–sillimanite–alkali feldspar–rutile–ilmenite–silicate melt–quartz (+ plagioclase for SW118) fields that border the rutile-out (to lower-*P*) and ilmenite-out (to higher-*P*) boundaries; the location of these fields varies with the 'O' content of the bulk composition. In both cases these boundaries shift up pressure with increasing oxygen values. The value chosen for the pseudosection calculations (O = 0·04) is relatively low, based on the low Fe^{3+} content of minerals in this sample (Tables 4 and 7). Peak metamorphic conditions for the Stillwell Hills as defined by the overlapping *P–T* space are $P = 7{\cdot}6$–$9{\cdot}4$ kbar at $T \geq 870$°C. An upper-*T* constraint is particularly difficult to obtain as the interpreted peak assemblage fields extend to very high temperatures. The absence of spinel-bearing assemblages in Si-undersaturated sample SW238 (see below) constrains peak-*T* to < 1000°C.

The contrast in the peak assemblages inferred for the Fe-rich (Fig. 6c) and Mg-rich (Fig. 6d) metapelites from Broka and Havstein Islands restricts the pressure range of high-grade conditions in that area. The peak assemblage for BH108 lies in the garnet–sillimanite–alkali feldspar–ilmenite–silicate melt–quartz ± spinel ± magnetite fields. An estimation of the amount of Fe^{3+} affects the stability of peak minerals spinel and magnetite. For this reason the larger spinel- and magnetite-absent field is included as part of the peak assemblage. For BH134, the narrow trivariant field garnet–cordierite–orthopyroxene–sillimanite–alkali feldspar–plagioclase–rutile–silicate melt–quartz best represents the peak assemblage. This sample locally lacks orthopyroxene and/or cordierite, and thus the orthopyroxene-absent (low-*P*) and cordierite-absent (high-*P*) fields are included here. Peak metamorphic conditions for Broka and Havstein Islands are estimated at $P = 7{\cdot}4$–$8{\cdot}5$ kbar at $T = 900$–1000°C.

The Mg-rich sample OG589 (Fig. 6f) contains orthopyroxene and garnet-rich domains with or without cordierite and sillimanite. Hence, cordierite and/or sillimanite may or may not have been part of the peak

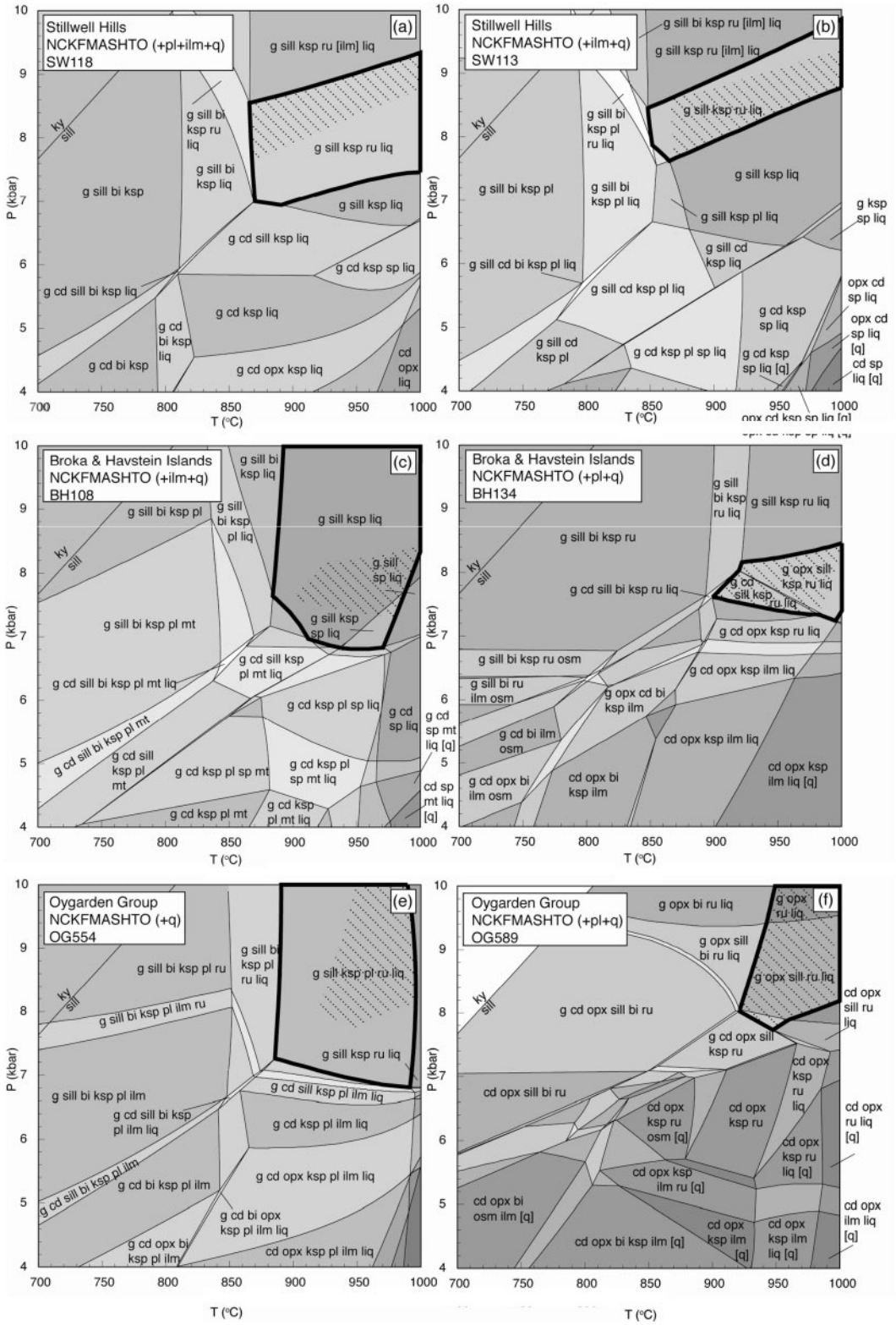

Fig. 6. *P–T* pseudosections for the Si-saturated metapelites from Kemp Land. (a)–(c) and (e) are Fe-rich samples (Assemblage I), and (d) and (f) are Mg-rich samples (Assemblage II). Fields with bold outline represent inferred peak metamorphic assemblages for each sample. Hatched area shows overlapping *P–T* space for each location. Mineral equilibria at low *T*, high *P* for OG589 have not been calculated as we infer that orthoamphibole may be stable in this range. The stability of this mineral cannot be currently calculated.

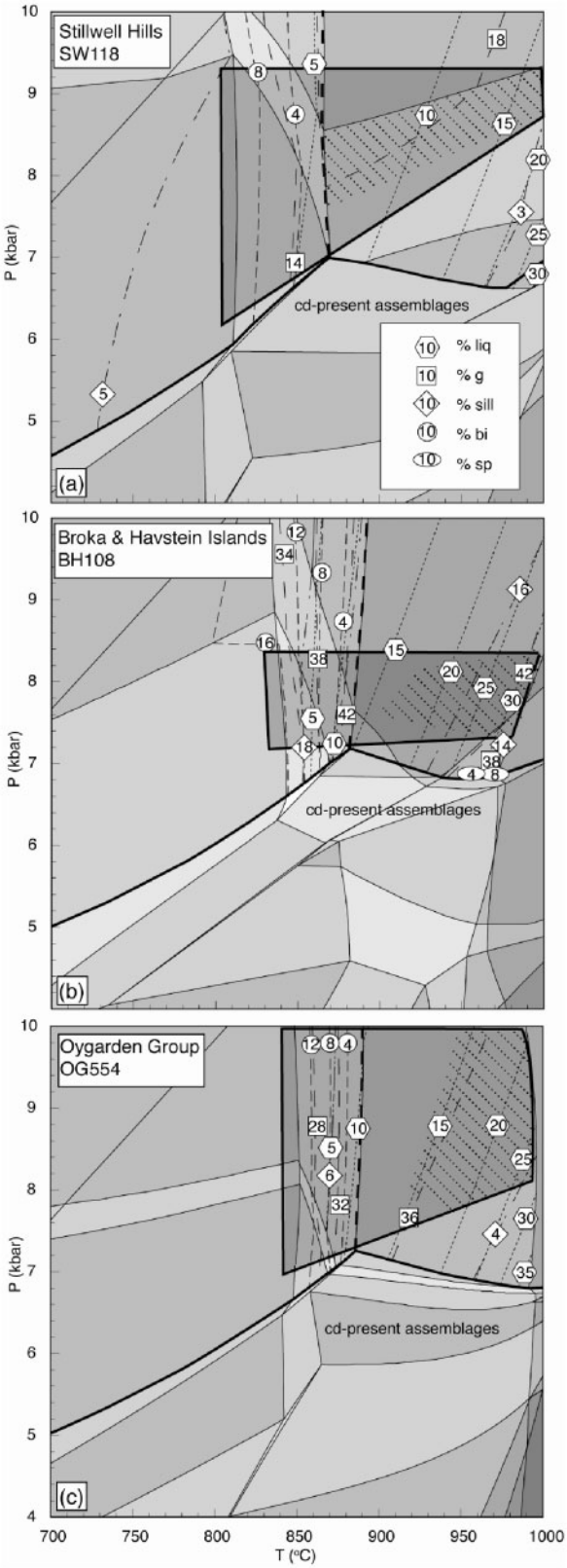

Fig. 7. (a)–(c) P–T pseudosections calculated for SW118, BH108 and OG554, respectively, with mineral mode contours, peak conditions (hatched area) and the limits of cordierite-in (bold line), biotite-in (dashed line) assemblages as discussed in the main text. A P–T trajectory that satisfies the observed post-peak mineral microstructures would pass through the area indicated by the dark shaded polygons with bold outlines. Assemblage field labels as in Fig. 6.

parageneses. The peak assemblage for OG589 is inferred to contain garnet–orthopyroxene–plagioclase–rutile–silicate melt–quartz ± cordierite ± sillimanite. The three (local) peak fields overlap with the garnet–sillimanite–alkali feldspar–plagioclase–rutile–silicate melt–quartz quinivariant field for the Fe-rich sample OG554 (Fig. 6e). The overlapping P–T space defines peak metamorphic conditions for the Oygarden Group of $P = 7{\cdot}7$–10 kbar at $T = 920$–990°C.

Post-peak P–T evolution

The retrograde history of the rocks must be considered in the context of the estimated peak conditions. In the case of the Si-saturated metapelites, reaction microstructures are limited. Assemblage I metapelites were particularly mineralogically insensitive to changes in P or T from peak conditions, as corroborated by the large P–T extent of peak assemblage fields across which there are very small (<5 mol %) changes in mineral modal abundances (Fig. 7). Assemblage II metapelites show some reaction microstructures but as they are influenced by local domainal chemistry they cannot be confidently represented by the calculated pseudosections. Although the post-peak trajectory is difficult to quantitatively constrain using these rocks, several limits on the retrograde P–T paths for the Kemp Land coastline can be interpreted. Figure 7a-c shows the calculated Assemblage I P–T pseudosections for the three areas (SW118, BH108 and OG554) with mineral mode contours for the assemblage fields of relevance. Superimposed on these diagrams are the peak conditions inferred in the previous section, as well as the upper-P limits to a retrograde path inferred from the absence of cordierite from post-peak assemblages. A P–T path for each of the three areas must cross the mineral proportion contours in such a way as to explain the growth of biotite and minor sillimanite at the expense of garnet. It is not possible to form biotite along an isothermal or near-isothermal decompressive path from the peak conditions in these pseudosections. To more tightly constrain the magnitude of cooling vs decompression within metapelites from Kemp Land we have integrated pseudosections calculated for Si-undersaturated rocks with petrographic observations (below).

P–T constraints from Si-undersaturated metapelites in the Stillwell Hills

P–T pseudosections for three Si-undersaturated metapelites from the Stillwell Hills were calculated (Fig. 8)

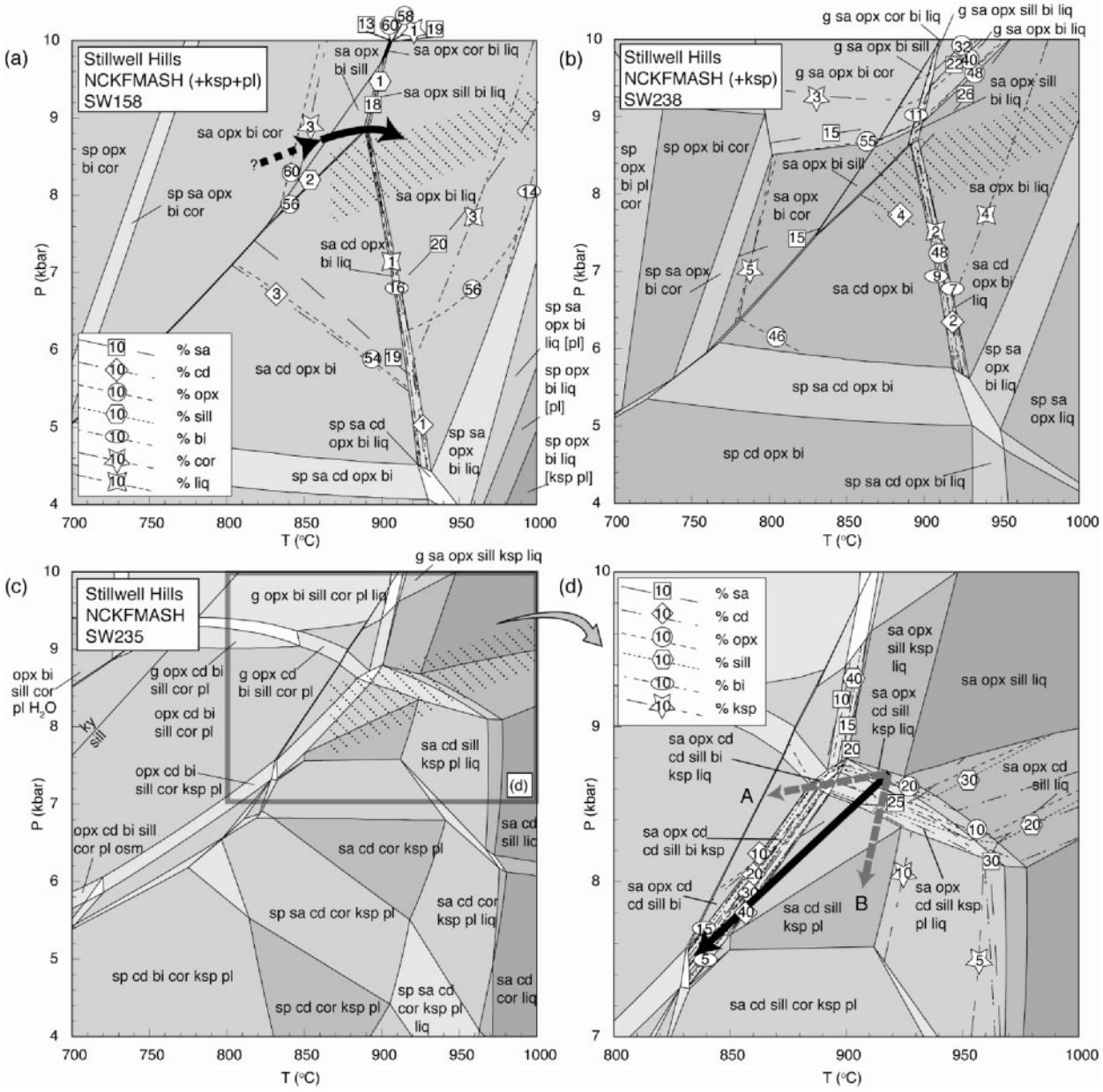

Fig. 8. *P–T* pseudosections calculated for Si-undersaturated metapelites from the Stillwell Hills. Peak metamorphic conditions as derived from the Si-saturated metapelites are shown as the hatched area. (a) A prograde *P–T* vector is inferred to cross the narrow trivariant sa + opx + bi + cor + sill + ksp + pl across which corundum becomes metastable in sample SW158. Mineral mode contours reflect an increase in sapphirine at the expense of corundum and orthopyroxene, consistent with the development of the sapphirine coronae, which completely isolate corundum from the peak assemblage. (b) An upper pressure and temperature limit to peak metamorphic conditions is set by the stability fields involving garnet and spinel, respectively; minerals that are absent from sample SW238. (c) A *P–T* pseudosection calculated specifically for the sill + opx breakdown microstructure in sample SW235 (Fig. 3). (d) The black arrow shows the retrograde *P–T* vector that best accounts for the rapid increase in cd and sa at the expense of sill and opx across the sa + opx + cd + sill + ksp + pl trivariant field. The increase in opx, sill and bi at the expense of cd and sa across the trivariant sa + opx + cd + sill + bi + ksp (below the solidus) is consistent with fine-grained textures observed in SW235 driven by fluid release from cordierite during breakdown. (For explanation of the dashed arrows labelled A and B see main text.)

and satisfactorily account for the three stages of sapphirine growth previously described, as discussed below.

Prograde and peak P–T evolution

To investigate the development of coronal sapphirine (association I) on corundum, sample SW158 was

modelled (Fig. 8a). These microstructures are very similar to those described from the Oygarden Group by Kelly & Harley (2004*a*). The peak conditions deduced from the Si-saturated metapelites encompass the assemblage sapphirine–orthopyroxene–biotite–alkali feldspar–plagioclase ± silicate melt ± cordierite. Sapphirine coronae on corundum are interpreted to have formed from the reaction between orthopyroxene and corundum to form sapphirine and sillimanite, consistent with the relative changes in mineral modes (Fig. 8a). The (melt-absent) assemblage orthopyroxene + corundum is predicted to be stable over a wide range of P–T conditions on this pseudosection (Fig. 8a), with corundum reacting out across a steep positive-sloped (effective) univariant to produce sillimanite. However, this diagram can only be crudely used to interpret the development of the sapphirine coronae. The extensive orthopyroxene + corundum fields can be expected to be restricted if melt were present prior to peak conditions. For the estimated bulk-rock composition, orthopyroxene + corundum + melt-bearing fields are restricted to $P > 9{\cdot}6$ kbar. Whereas it may be difficult to model prograde textures in such high-grade rocks, this pseudosection allows a qualitative assessment of the prograde P–T path in the Stillwell Hills, immediately prior to peak conditions. Coarse-grained sapphirine coronae that in some cases completely pseudomorph the corundum are inferred to have developed along a prograde heating path between $T \approx 800$°C and 900°C, to peak conditions. The absence of cordierite from the reaction microstructure probably indicates near-peak $P > 7{\cdot}6$ kbar.

Figure 8b is a P–T pseudosection appropriate to sample SW238, which contains sapphirine laths minimally consumed by overprinting assemblages involving fine-grained sillimanite and/or cordierite coronae (sapphirine of association II). The stability of garnet in this pseudosection at $P > 8{\cdot}4$ kbar places a robust limit to upper-P conditions. The absence of spinel in these Mg-rich rocks places a further upper-T limit (<1000°C) on the conditions in the Stillwell Hills. More Fe-rich compositions would encounter garnet-bearing fields at lower P and spinel-bearing fields at lower T. The development of minor retrograde sillimanite and narrow cordierite coronae are consistent with a decompressive-cooling path. However, as the bulk composition is derived from XRF analysis, the interpretation of this diagram should be limited to peak conditions that coincide with peak P–T conditions constrained from Si-saturated metapelites (hatched area: Fig. 8).

Post-peak P–T *evolution*

The post-peak P–T trajectory for metapelites from the Stillwell Hills can be illustrated using the sillimanite reaction textures in SW235. Sapphirine + cordierite symplectites that enclose coarse-grained sillimanite are the most notable example of sapphirine in association III. An element map of the reaction texture between sillimanite and orthopyroxene (Fig. 3) was used for the calculation of an appropriate bulk composition. The pseudosection for this rock is shown in Fig. 8c and d. The observed sequence of mineral reactions is consistent with a decompressive-cooling path passing through the sapphirine–orthopyroxene–cordierite–sillimanite–plagioclase–alkali feldspar–silicate melt trivariant field to sub-solidus conditions (arrow in Fig. 8d). Increases in the abundance of sapphirine and cordierite across this field occur at the expense of sillimanite and orthopyroxene. This is consistent with observed textures involving the breakdown of peak sillimanite ($sill_1$) and orthopyroxene (opx_1) to produce sapphirine (sa_2) and appreciable cordierite (cd_2) (Fig. 3). The ratio of cordierite:sapphirine increases along this path to about 40:25, consistent with the observed cordierite moats around the cordierite + sapphirine symplectites.

Fine-grained orthopyroxene (opx_2), sillimanite ($sill_2$) and biotite (bi_2; Fig. 3) indicate subsequent partial replacement of the symplectic minerals cordierite (cd_2) + sapphirine (sa_2) ± alkali feldspar (ksp_2). We infer that this reaction was driven by the breakdown of hydrous cordierite and is predicted to occur across the trivariant field sapphirine–orthopyroxene–cordierite–sillimanite–biotite–plagioclase–alkali feldspar along the P–T path to $T \approx 840$°C at $P \approx 7{\cdot}5$ kbar (Fig. 8d). Modal contours indicate the production of biotite, orthopyroxene and sillimanite at the expense of cordierite, sapphirine and alkali feldspar consistent with the observed texture.

An integrated *P*–*T* path

Si-saturated and Si-undersaturated samples from the Stillwell Hills provide consistent evidence for a prograde heating trajectory to peak conditions of $T = 870$–1000°C at $P = 7{\cdot}6$–$9{\cdot}4$ kbar, followed by decompression-cooling to $T \approx 840$°C at $P \approx 7{\cdot}5$ kbar. As a range of peak conditions is representative of assemblages preserved in the Stillwell Hills, P–T paths with differing (including curved) slopes between peak metamorphic conditions and $T \approx 840$°C, $P \approx 7{\cdot}5$ kbar are consistent with the changes in mineral proportions and growth of retrograde minerals. Shallow (cooling-dominated) retrograde paths do not allow for the increase in cordierite and sapphirine modes observed in the Si-undersaturated metapelites (path A in Fig. 8d). Alternatively, steep (decompression-dominated) retrograde paths do not intersect biotite-bearing fields and instead predict the consumption of orthopyroxene (path B in Fig. 8d). A decompressive-cooling path with $dP/dT \approx 15$–20 bar/°C is consistent with the post-peak mineral parageneses in the Stillwell Hills (Fig. 9a and b). This P–T path also matches the trend of decreasing y(opx) for porphyroblastic orthopyroxene (Fig. 9b). The post-peak P–T trajectory for the Stillwell Hills is also consistent with the development of cordierite rims around garnet and/or orthopyroxene, and the growth of

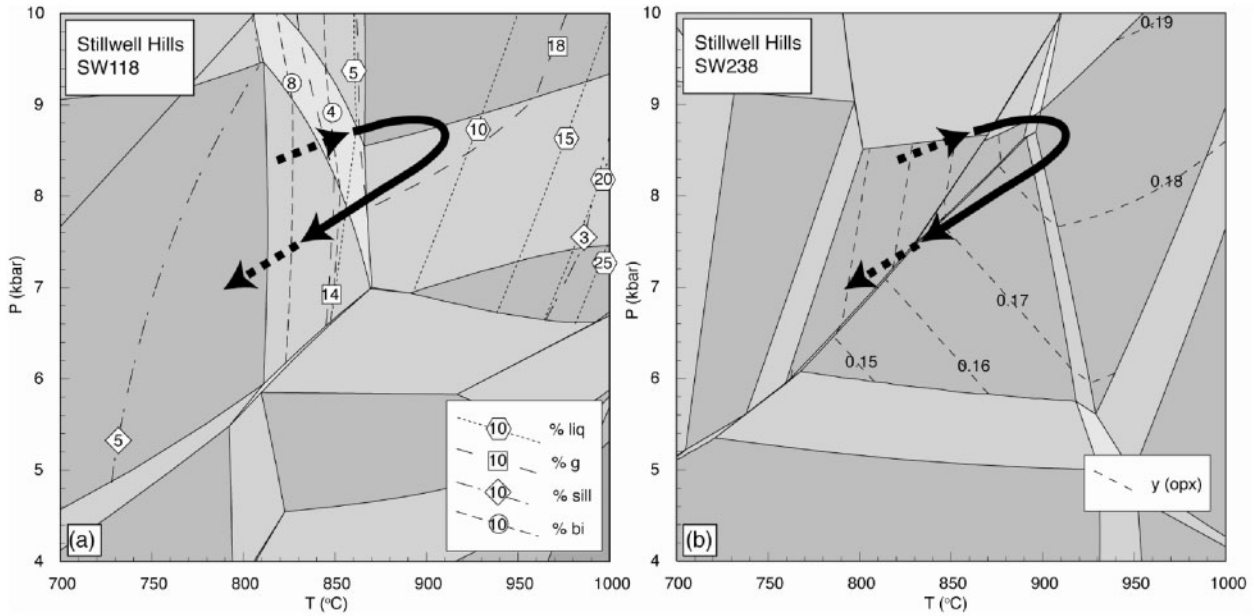

Fig. 9. *P–T* path inferred for Si-saturated (a) and Si-undersaturated (b) metapelites from the Stillwell Hills (for explanation see text). Assemblage field labels as for Figs 6a and 8b.

retrograde biotite in metapelites from Broka and Havstein Islands and the Oygarden Group, and thus may be more widely applicable for the Kemp Land terrane. A moderately sloped *P–T* path is in contrast to near-ITD paths inferred for Turbulence Bluffs (Ellis, 1983), the Oygarden Group (Kelly & Harley, 2004*a*) and Broka and Havstein Islands (Schröter, 2006).

MONAZITE (Th+U)–Pb GEOCHRONOLOGY

Chemical dating of monazite is now a well-established method (e.g. Montel *et al.*, 1996; Cocherie *et al.*, 1998; Crowley & Ghent, 1999; Williams *et al.*, 1999; Williams & Jercinovic, 2002; Pyle *et al.*, 2005). The chemical composition of monazite grains (Fig. 10) was analysed *in situ* via mapping and spot analysis using a Cameca SX-51 EMP equipped with four wavelength-dispersive spectrometers at the University of Adelaide. Elemental mapping of Y, Th, U and Pb in monazite (Williams & Jercinovic, 2002; Yang & Pattison, 2006) was performed on larger monazite grains to detect chemical zonation (Figs 11 and 12). The position of spot analyses utilizes the chemical zonation patterns from elemental maps. Operating conditions and the methodology of monazite age calculations are detailed in the Appendix. Age calculations use the measured Th, U and Pb contents and involve a multi-stage procedure outlined by Kelsey *et al.* (2003*a*) and summarized in the Appendix.

Assumptions in the derivation of monazite ages

Chemical ages calculated from monazites are based on several assumptions: (1) common Pb has a negligible contribution to the total amount of Pb in the system; (2) the system has remained closed (i.e. no Pb loss from the system since passing through the closure temperature); (3) an individual spot analysis represents a single age; (4) if individual ages are pooled for the determination of a 'mean', they represent a single age-population.

The amount of common Pb relative to total Pb in monazites is low and provides the strongest validation of the chemical dating technique (Parrish, 1990). The diffusivity of Pb in monazite has been experimentally determined to be low, even at high *T*, and comparably sluggish to Pb diffusion in zircon (Cherniak *et al.*, 2004). Estimates for the closure temperature of Pb diffusion in monazite are varied and are likely to be influenced by a number of factors including the composition of the monazite itself, grain size, textural context, rate of cooling, recrystallization, availability of fluids or melt, bulk composition and deformation (e.g. Parrish, 1990; DeWolf *et al.*, 1993; Zhu & O'Nions, 1999*b*; Montel *et al.*, 2000; Fitzsimons *et al.*, 2005). The presence of several populations with calculated ages prior to the age of the last granulite-facies metamorphic event in the Oygarden Group indicates that the interaction of factors such as these is complex (see also Kelly & Harley, 2004*b*). The significance of a spectrum of ages is discussed in more detail below.

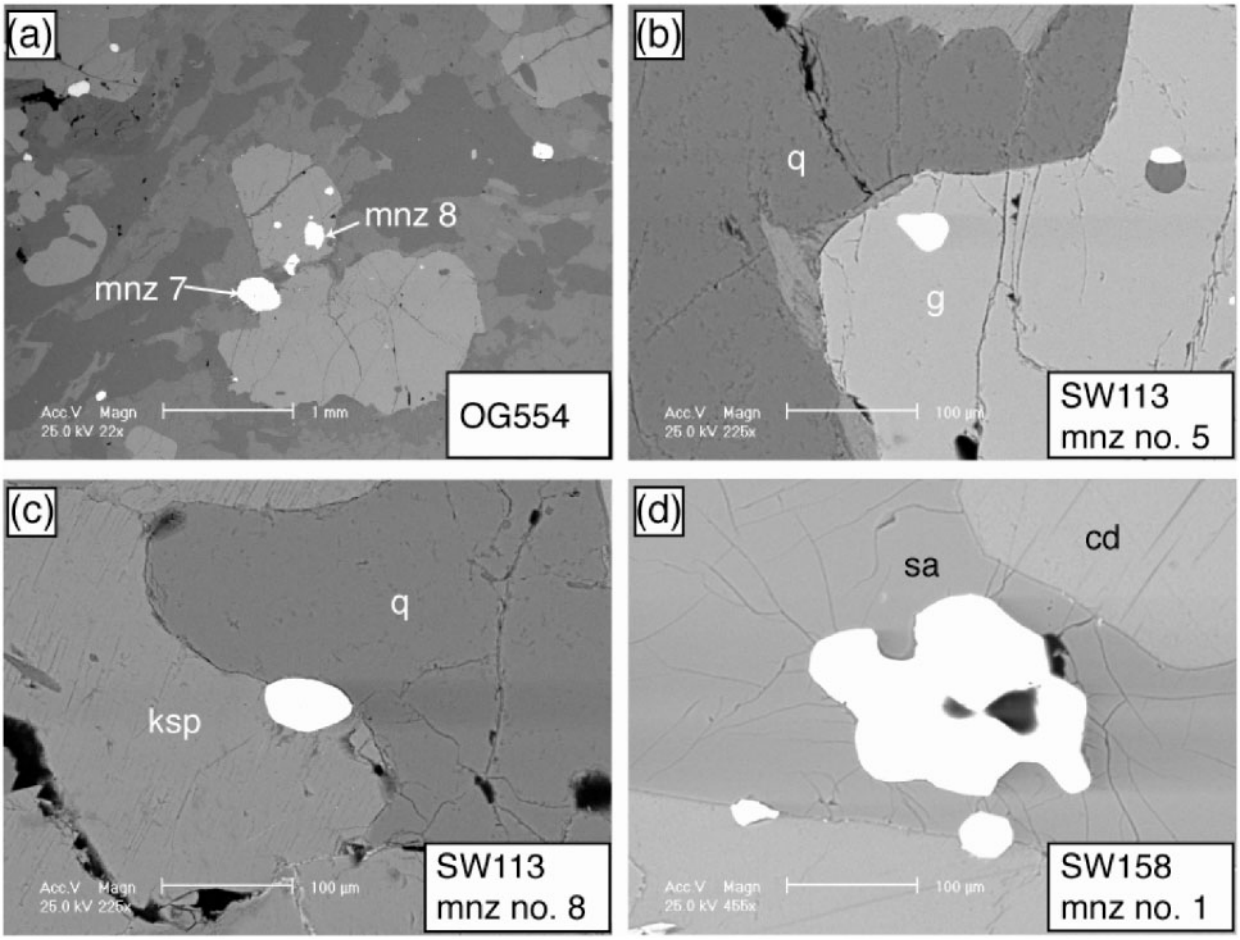

Fig. 10. Backscattered electron images of textural settings for representative monazites analysed from Kemp Land. (a) Monazite from sample OG554 from the Oygarden Group included in garnet (mnz 8) and in contact with matrix minerals (mnz 7). (b) Typical small and rounded monazite from sample SW113 from the Stillwell Hills included in garnet. (c) Monazite from sample SW113 in contact with alkali feldspar and quartz. (d) Monazite from sample SW158 in the Stillwell Hills with embayed grain boundaries, enclosed within sapphirine.

(U + Th)–Pb dating results

Oygarden Group

The monazite grains analysed in sample OG554 from the Oygarden Group include three grains (up to 200 μm) completely enclosed within porphyroblastic garnet and one grain (up to 340 μm) partially surrounded by garnet and in contact with matrix minerals alkali feldspar and quartz (Fig. 10a). Element maps for the larger two grains (Fig. 11) reveal zonation in Th and Y. Eighty-eight analyses of four monazites in sample OG554 show a large spread of spot ages (these analyses are available as Table 1 of the Electronic Appendix, available for downloading at http:/www.petrology.oxfordjournals.org).

The oldest, *c.* 2350–1950 Ma, ages (Group 1; Fig. 13) from a monazite included in garnet (Table 1 of the Electronic Appendix; mnz 8) are concentrated towards a Pb- and Y-rich core region (Fig. 11a). This domain is interpreted as an inherited core. The limited number of analyses does not permit the calculation of a statistically viable mean age for this core.

A large range of ages between *c.* 1800 and 1100 Ma (Group 3; Fig. 13) was collected from monazites located within garnet and the rock matrix (Fig. 13d). Monazite inclusions in garnet give an older age population that overlaps with *c.* 1400 Ma matrix monazite grains (Fig. 13d). The main *c.* 1650–1250 Ma population contains several sub-populations, even considering textural settings. ThO_2 and UO_2 contents show marked variation ($\leq$3·17 wt % and $\leq$2·70 wt %, respectively). There are no distinct major or trace element chemical groups in this age range population, rendering the data difficult for the calculation of a statistically meaningful age.

The youngest group of ages in monazites from the Oygarden Group (Group 2; Fig. 13) are in the range *c.* 1000–800 Ma (Fig. 13b). Smaller monazites preserve predominantly young ages (mnz 4 and mnz 5; Table 1 of the Electronic Appendix), despite sometimes being

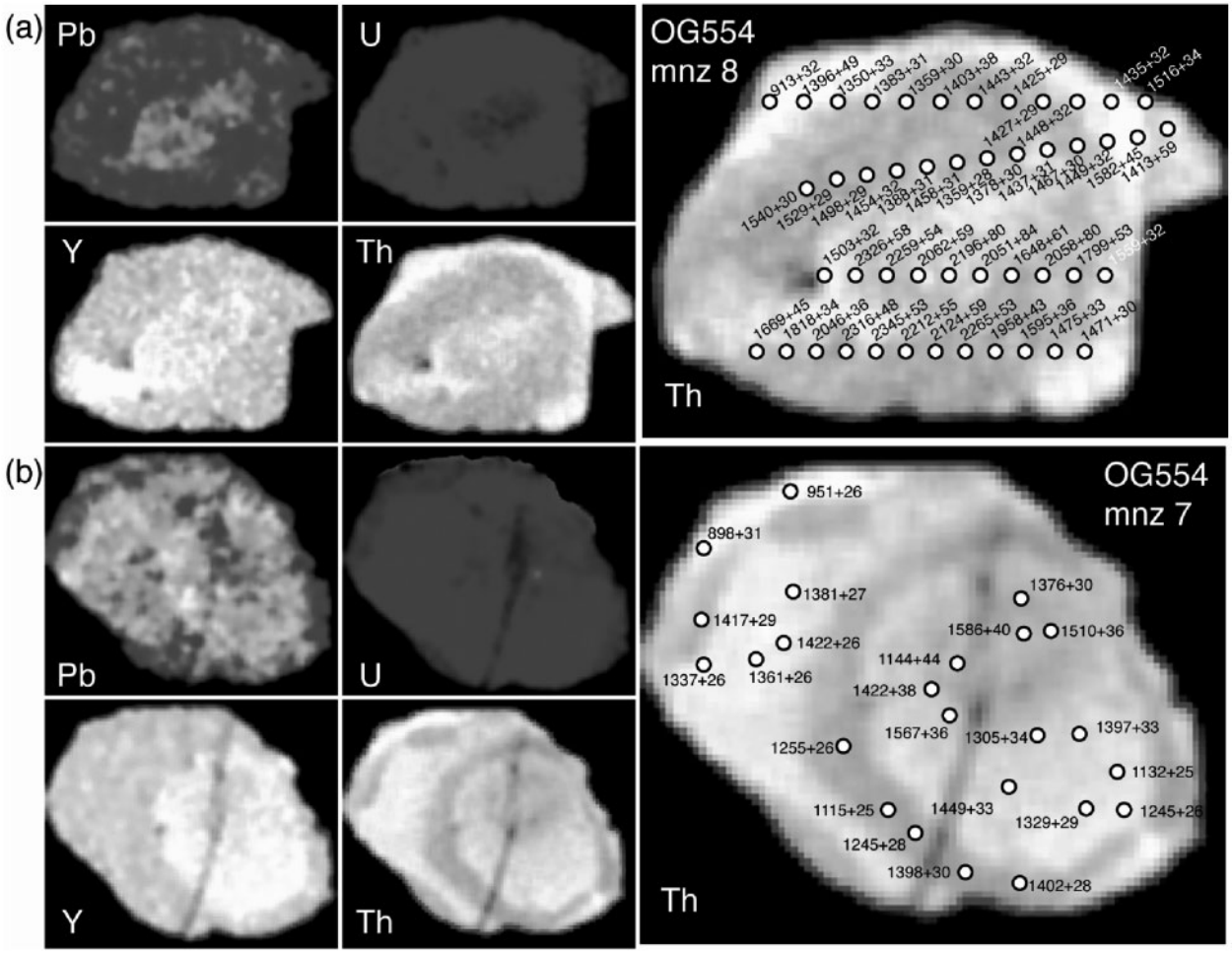

Fig. 11. Element maps and spot ages in large monazites from the Oygarden Group. (a) A core region in mnz 8 from OG554 appears to correlate with older spot ages (bright areas indicate high concentrations). (b) Concentric zoning in mnz 7 from sample OG554 is revealed in the Th map. The innermost domain yields the oldest ages; however, a large crack running through the centre of the grain may be responsible for local composition variation.

enclosed by garnet. Three analyses on the rims of larger monazite grains also give ages in this range (Fig. 11). The relatively large range in UO_2 and ThO_2 (0·52–1·36 wt % and 5·50–9·66 wt %, respectively) occurs in a monazite in garnet that is surrounded by cracks that extend to the rock matrix (mnz 4). Fifteen of the 16 analyses in this group (excluding the youngest age) define a single population with a tanh age (see the Appendix) of 930 ± 15 Ma, indistinguishable from the Mikhail age (see the Appendix) and within the 95% confidence limit (Table 10; Fig. 13c).

Stillwell Hills

Monazite grains in Fe-rich, Si-saturated sample SW113 from the Stillwell Hills are < 70 μm across (commonly < 50 μm) and occur both as inclusions in garnet (Fig. 10b) and in the rock matrix (Fig. 10c). Variation in Th, U and Pb contents within a single monazite grain can be marked (Table 1 of the Electronic Appendix); monazites included in garnet have a range of ThO_2 (5·06–12·89 wt %) and PbO (0·28–0·60 wt %) and comparable UO_2 contents (0·37–0·76 wt %) to monazite in the matrix (5·14–16·97 wt % ThO_2, 0·28–0·75 wt % PbO, 0·33–0·67 wt % UO_2). Eighty-five analyses of 20 monazite grains have a spread of individual ages from 1033 to 830 Ma (Table 1 of the Electronic Appendix). Monazite inclusions in garnet define a population with a mean age of 943 ± 8 Ma (Table 10; Fig. 14a and c). The matrix population has a mean age of 929 ± 7 Ma (Table 10; Fig. 14b and c).

Monazite from Mg-rich, Si-undersaturated sample SW158 occurs as inclusions in sapphirine (Fig. 10d), at grain boundaries between orthopyroxene and cordierite, and within corundum. Large monazite grains show complex zoning, particularly in Th and Y (Fig. 12). Monazite inclusions in sapphirine have a larger range in ThO_2 (≤15·11 wt %) and PbO (≤0·61 wt %) than

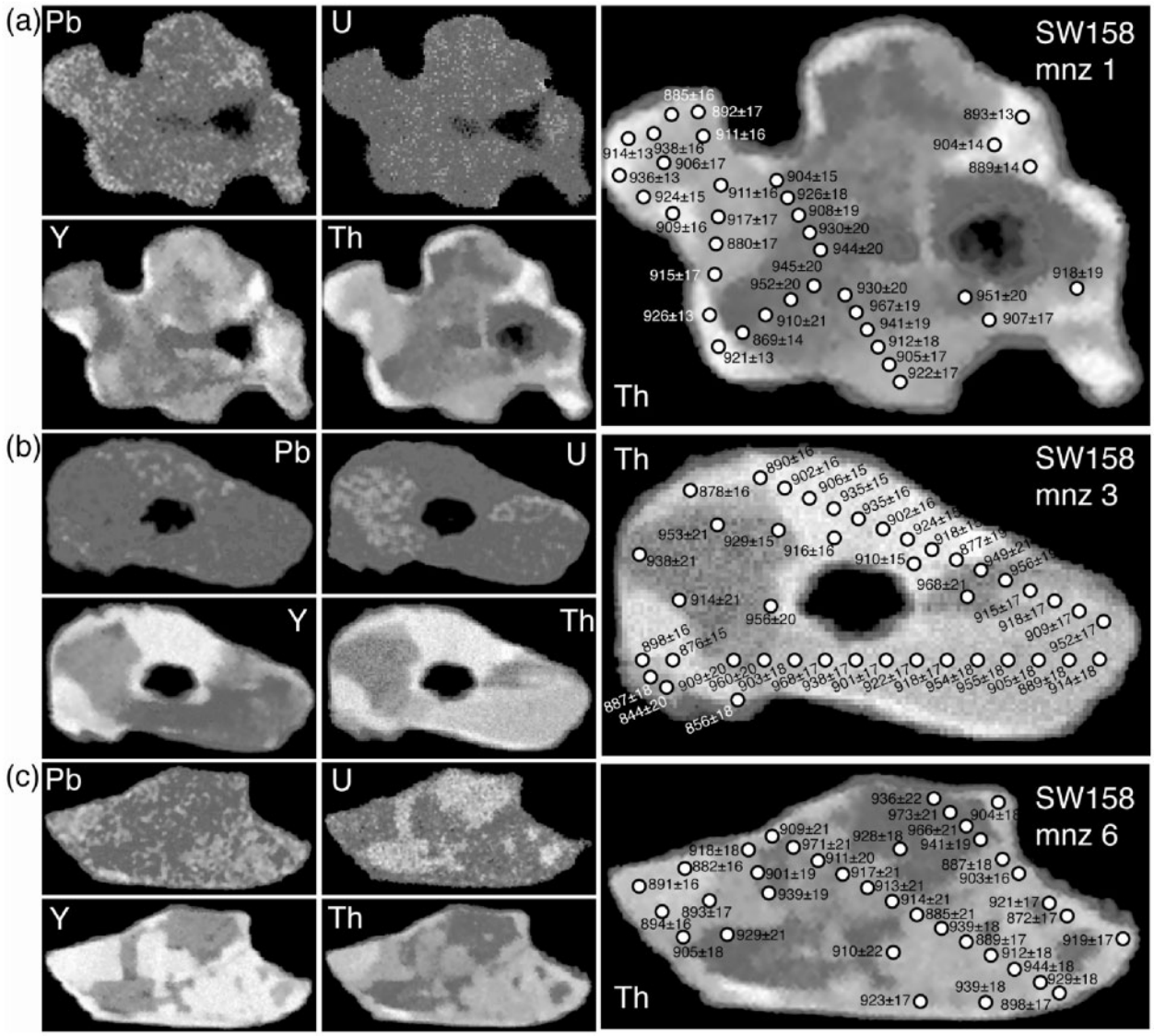

Fig. 12. Element maps and spot ages in large monazites from the Stillwell Hills. (a)–(c) Patchy zoning and embayed rims in monazite from sample SW158 indicate recrystallization of monazite during metamorphism. Although there is not a consistent correlation, domains of Th enrichment may yield younger ages.

monazite in contact with orthopyroxene and cordierite ($ThO_2 \leq 9{\cdot}93$ wt % and PbO $\leq 0{\cdot}41$ wt %). The variability in UO_2 contents in sapphirine-hosted monazite is slightly less ($UO_2 \leq 0{\cdot}34$ wt %) than in monazite associated with orthopyroxene and cordierite ($UO_2 \leq 0{\cdot}46$ wt %). Very small (<60 μm) and cracked monazite grains occurring as inclusions in corundum yield poor data. A single analysis (mnz 12) indicates that monazite in corundum may be enriched in UO_2 (1·43 wt % compared with 0·47–0·93 wt %) with comparable ThO_2 and PbO contents to other analysed monazite. One hundred and fifteen analyses from four monazites have a spread of ages between 973 and 844 Ma (Table 1 of the Electronic Appendix). Despite the intricate zonation observed in the large monazite grains, the individual spot ages from the two textural settings define tight populations with mean ages of 918 ± 3 Ma (in sapphirine; Table 10, Fig. 14d and f) and 914 ± 4 Ma (with orthopyroxene and cordierite; Table 10, Fig. 14e and f).

DISCUSSION

Pre-Rayner Orogeny monazite ages in Kemp Land

The oldest ages, *c.* 2350–1950 Ma, from a core in monazite 8 from the Oygarden Group might indicate a maximum age for the sedimentation of the protolith, provided this is

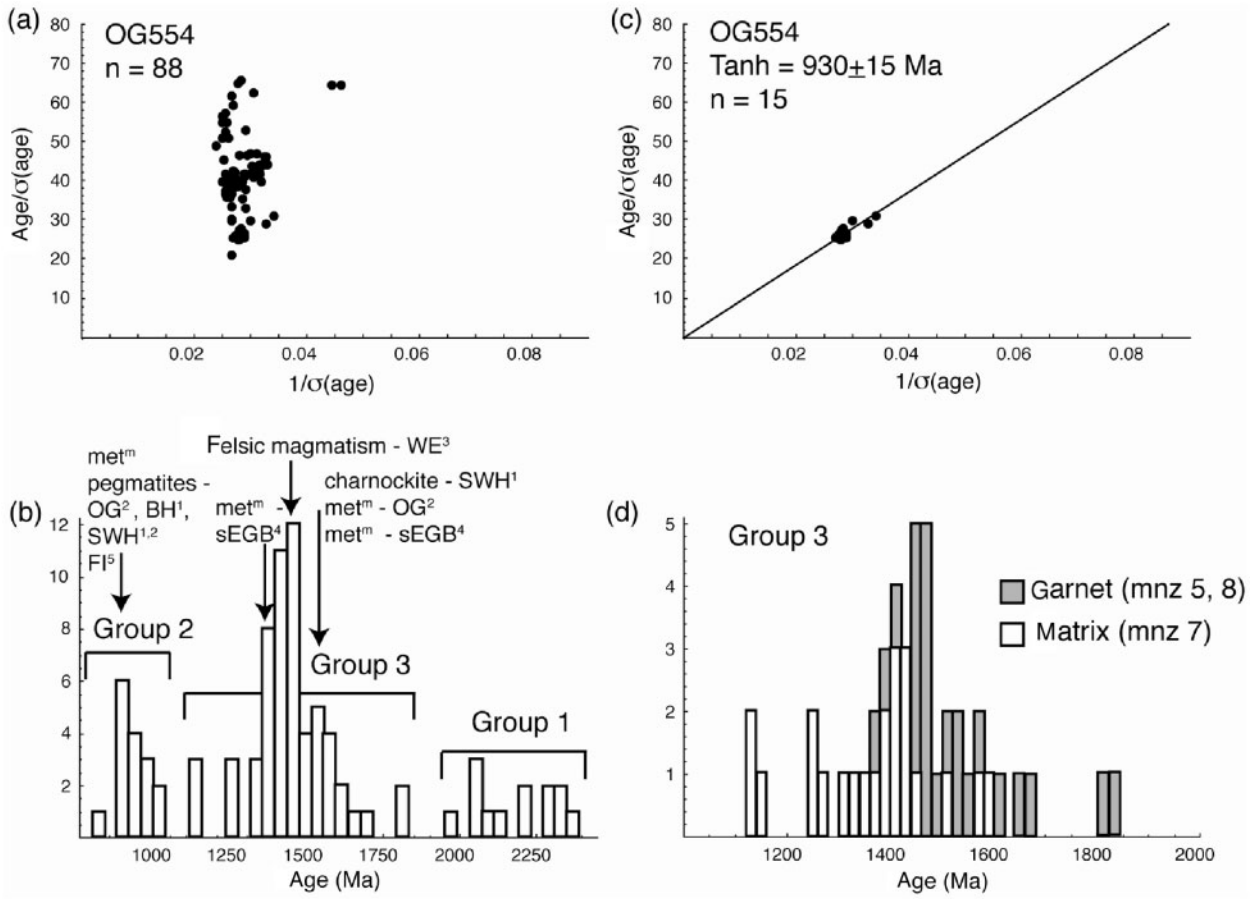

Fig. 13. Monazite age data for the Oygarden Group. All errors are 2σ. (a) Individual ages given by the filled circles for sample OG554 show a large spread reflecting a complex tectonothermal history. σ(age) is the analytical uncertainty (from counting statistics) associated with each analysis. (b) Three broad age groupings (discussed in text) are apparent in the monazite age histogram. Previously published ages of magmatism and metamorphism in the Oygarden Group (OG), Stillwell Hills (SWH), Broka and Havstein Islands (BH) and Fold Island (FI) in Kemp Land are indicated. Comparisons with age data from Group 3 from Western Enderby Land (WE) and the southern Eastern Ghats Belt (sEGB) in India are also shown. References: 1, Halpin *et al.* (2005); 2, Kelly *et al.* (2002); 3, Black *et al.* (1987); 4, Mezger & Cosca (1999); 5, Grew *et al.* (1988). All ages are mineral ages (zircon, monazite or allanite). (c) Fifteen analyses of Group 2 monazite ages define an isochron with a tanh age of 930 ± 15 Ma. (d) Monazite ages from within garnet have a main population that is *c.* 50 Myr older than the main population from matrix monazite.

Table 10: Monazite mean ages

Sample	Group/setting	*n*	Tanh age (Ma) (2σ error)	Mikhail age (Ma) (2σ error)	Sig. fit	Limit for 95% conf.
OG554	Group 2	15	930 ± 15	932 ± 18	1·1	1·3
SW113	in garnet	37	943 ± 6	936 ± 14	1·2	1·2
	in matrix	48	929 ± 7	919 ± 9	1·2	1·2
SW158	in sapphirine	36	918 ± 3	915 ± 5	1·3	1·2
	in matrix	78	914 ± 4	916 ± 4	1·5	1·1

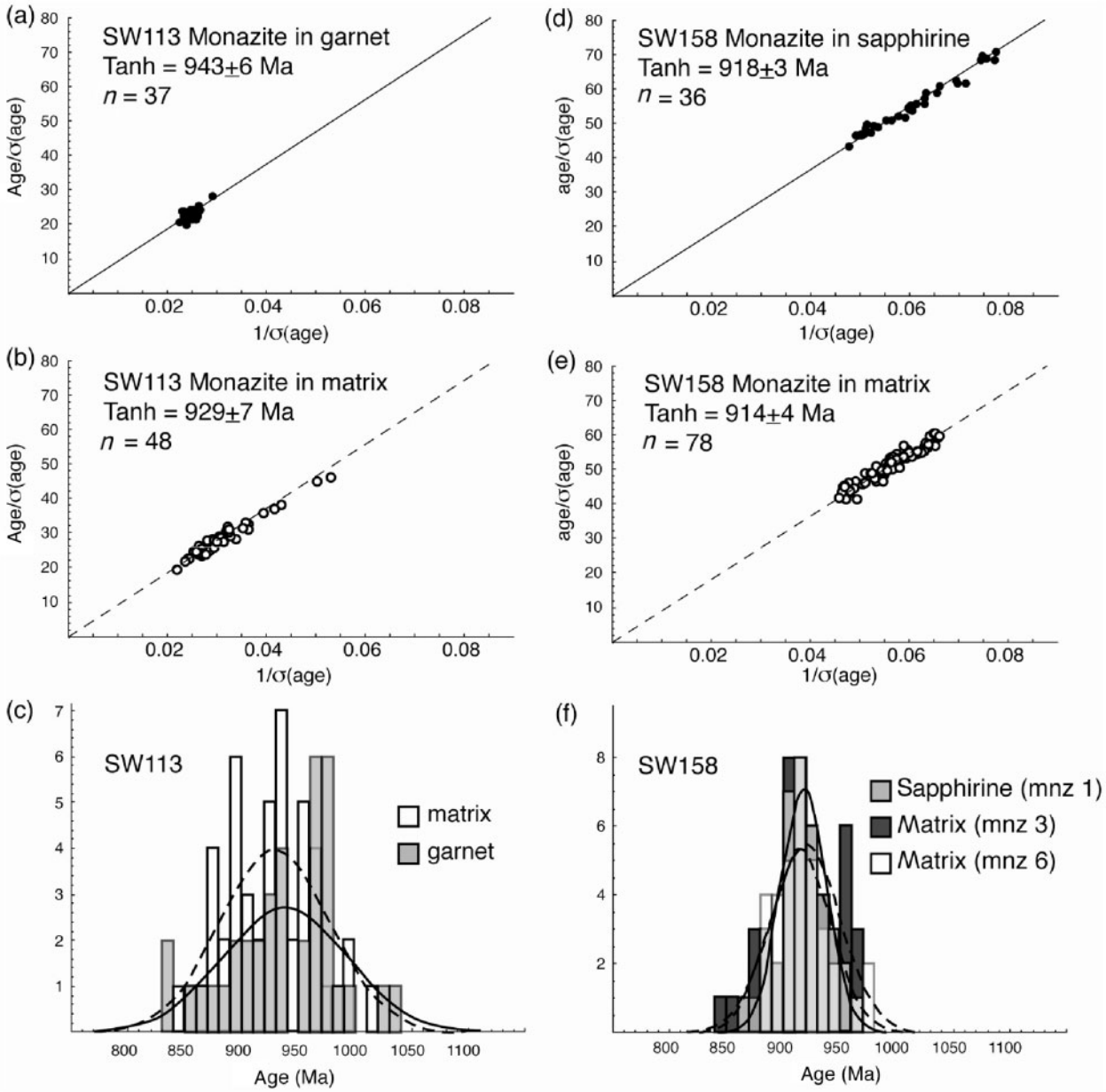

Fig. 14. Monazite age data for the Stillwell Hills. All errors are 2σ. (a) Monazite within garnet in sample SW113 defines a tight cluster at 943 ± 6 Ma. (b) Monazite that occurs in the matrix yields a (significantly) younger age of 929 ± 7 Ma. (c) A monazite age histogram reveals the skew to older ages for monazite included in garnet. Superimposed are the tanh age curves for monazite within garnet (continuous curve) and within the matrix (dashed curve). (d) A regression for monazite ages within sapphirine (mnz 1) for sample SW158 yields an age of 918 ± 3 Ma. (e) Monazite grains in the matrix (mnz 3 and mnz 6) have an age of 914 ± 4 Ma. (f) The monazite ages from the textural populations for sample SW158 are tightly constrained *c.* 920–915 Ma on the monazite age histogram. Tanh curves for monazite in sapphirine (continuous curve) and in the matrix (dashed curves) are indistinguishable within error.

a true indication of a detrital age and not an artefact of partial resetting. The extensive population of ages particularly *c.* 1400 Ma (monazite in the matrix) and *c.* 1450 Ma (monazite included in garnet) and a skew towards ages *c.* 1650–1500 Ma (Fig. 13d) suggest growth or recrystallization of monazite over an extended period of time. On the basis of U–Pb zircon ages from orthogneiss, a *c.* 1600 Ma thermal event occurred in the Oygarden Group (Kelly *et al.*, 2002, 2004) and charnockite was emplaced before *c.* 1550 Ma in the Stillwell Hills (Halpin *et al.*, 2005). The *c.* 1650–1500 Ma sub-population of ages in monazite is thus interpreted to relate to the intrusion of the charnockite in the Stillwell Hills. A Sm–Nd garnet age of *c.* 1560 Ma from Tonagh Island (Owada *et al.*, 2003)

could indicate that parts of the Napier Complex were also affected by an event at this time.

The chemical method of (U + Th)–Pb monazite analysis does not allow for consideration of any degree of discordance for the *c.* 1450–1400 Ma population and thus we are unable to discern whether these data: (1) indicate a separate *c.* 1450–1400 Ma thermal event (or indeed several closely spaced events); or (2) are a consequence of the partial resetting of older ages during a younger (Rayner Orogeny?) event. In the case of monazite 7, ages between *c.* 1450 and 1115 Ma occur across broad zones of distinct zonation particularly in Y and Th (Fig. 11b). The replication of these ages in three out of the four monazites analysed, including monazite within garnet, is most consistent with the first interpretation. However, such mid-Mesoproterozoic ages are rare in the Rayner Complex. Several similar U–Pb zircon ages have been reported for felsic intrusive rocks (*c.* 1488 Ma, 1465 Ma and 1425 Ma) in western Enderby Land (Black *et al.*, 1987; Fig. 13b). The age of the extensive dyke swarm in Kemp Land is only poorly constrained but may offer an alternative source for a thermal event of this age. These dykes are present as deformed relicts in *c.* 1600 Ma charnockite in the Stillwell Hills. If their correlation with the 1190 ± 200 Ma Amundsen dyke swarm (Sheraton & Black, 1981) in the Napier Complex is correct, this may suggest emplacement between 1400 and 1000 Ma.

Several comparisons can also be made with mineral ages from the Eastern Ghats Belt in India (EGB; Fig. 13b), which is assumed to have been located near the Kemp Land coastline, prior to the break-up of Gondwana. Felsic magmatism and metamorphism occurred *c.* 1650–1600 Ma and *c.* 1350 Ma in the Western Charnockite Zone, south of the Godavari Rift (monazite and allanite U–Pb ages; Mezger & Cosca, 1999). Pb-isotope analyses of feldspars from metasediments in this region show a tight array close to a *c.* 1500 Ma isochron (Rickers *et al.*, 2001*a*). Further north, *c.* 1450–1400 Ma Sm–Nd whole-rock isochron ages are interpreted to represent the intrusion of protoliths to mafic granulite and leptynite at Rayagada (Shaw *et al.*, 1997) and *c.* 1400 Ma U–Pb zircon ages may indicate the intrusion of basic melts in the Anakapelle region (Jarick, 2000, as quoted by Rickers *et al.*, 2001*b*). Comparisons between the Kemp Land coast and the EGB are complicated by apparently different tectonothermal histories for the regions north and south of the Godavari Rift, and mineral ages from the southern EGB do not record evidence of *c.* 1000–900 Ma disturbance (Mezger & Cosca, 1999; Rickers *et al.*, 2001*a*).

P–T–t path for the Rayner Orogeny in Kemp Land

Monazite analyses from samples from both the Oygarden Group and the Stillwell Hills yield mean ages *c.* 940–915 Ma. Ages *c.* 940 Ma come from monazite enclosed in garnet, which is shielded from resetting of the U–Th–Pb system (e.g. DeWolf *et al.*, 1993; Montel *et al.*, 2000). Garnet-hosted monazite associated with fractures that connect monazite grains to the matrix may have resulted in a bias towards younger ages; thus, we suggest peak metamorphism occurred at or before *c.* 940 Ma. Although older ages are present in monazite from the Oygarden Group (Kelly & Harley, 2004*b*; this study), mineral assemblages in the metapelites must represent conditions associated with the Rayner Orogeny as reaction textures in these rocks are undeformed by later deformation (see Kelly & Harley, 2004*a*). Further, smaller monazites give predominantly Neoproterozoic ages. We interpret these ages to represent growth and/or recrystallization of monazite during the Rayner Orogeny.

The difference in mean age between monazites from samples SW113 (*c.* 940–930 Ma) and SW158 (*c.* 920–915 Ma) may reflect the textural context and morphology of the monazites chosen for analysis, as well as bulk-rock composition (e.g. Fitzsimons *et al.*, 2005). 'Patchy' zoning, as observed in monazite grains from SW158, has been reported in other studies (e.g. Poitrasson *et al.*, 1996; Hawkins & Bowring, 1997; Bingen & van Breemen, 1998; Ayers *et al.*, 1999; Zhu & O'Nions, 1999*a*, 1999*b*; Townsend *et al.*, 2001). Monazite age data from SW158 indicate that in many cases there is not a link between the composition and age of the monazite. This implies that *in situ* recrystallization in monazite from sample SW158 is probably more responsible for the spread in ages across a single grain than new growth (e.g. Cocherie *et al.*, 1998). Further, curved grain boundaries are consistent with inward-directed secondary replacement and/or resorption of the monazite (Bingen & van Breemen, 1998; Zhu & O'Nions, 1999*b*). These observations suggest that recrystallization of monazite during the Rayner Orogeny occurred until *c.* 915 Ma in the Stillwell Hills, possibly related to the crystallization of remaining partial melt. This time-frame for the Rayner Orogeny derived from monazite data is coeval with that deduced from *c.* 930–920 Ma zircon ages in the Oygarden Group (Kelly *et al.*, 2002; Fig. 13b), *c.* 940 Ma metamorphism at Broka and Havstein Islands (Halpin *et al.*, 2005) and *c.* 915 Ma concordant U–Pb ages from 'metamorphic-type' zircon cores and rims from the Stillwell Hills (Kelly *et al.*, 2002). These data are also comparable with a zircon U–Pb age of 940 ± 80 Ma from a late or post-tectonic pegmatite from Fold Island (Grew *et al.*, 1988).

Petrographic observations and thermodynamic modelling of peak mineral assemblages in metapelites from the Kemp Land coast suggest that metamorphic conditions reached $T = 870$–$990^{\circ}C$ at $P = 7{\cdot}4$–10 kbar during the *c.* 940–915 Ma Rayner Orogeny. Estimates of peak-*P* for the three locations studied are within error; however, lower-*P* estimates from the Stillwell Hills and Broka

and Havstein Islands are consistent with the coastline representing a tilted crustal block. This crustal profile may be dissected by younger thrust faults, although large-scale faults are not observed because of paucity of outcrop along the coast.

Peak P–T conditions for the Stillwell Hills, Broka and Havstein Islands and the Oygarden Group derived in this study differ from previous estimates, as they do not rely on compositions of coexisting minerals. Previous peak-T estimates from Kemp Land constrained by geothermometry may underestimate peak-T, ultimately resulting in an ITD-dominated post-peak P–T path (e.g. Ellis, 1983). Derivation of a P–T path from simplified petrogenetic grids such as that in the MgO–Al_2O_3–SiO_2 (MAS) system presented by Kelly & Harley (2004*a*) would require decompression from high pressures ($P \approx 13$ kbar) to account for observed mineral reaction microstructures, inconsistent with thermobarometry undertaken on the rocks (Kelly & Harley, 2004*a*). A 'bulk rock integrated' approach, which incorporates a chemically realistic model system used to derive a clockwise P–T–t path in this study, suggests that a decompressive-cooling post-peak trajectory best describes the growth of retrograde mineral assemblages in Kemp Land. Tectonic implications of a moderately sloped post-peak P–T path (compared with a near-ITD P–T path) suggest that rapid post-collisional uplift at sustained high-T need not be invoked for the Kemp Land terrane.

CONCLUSIONS

The apparent coexistence of texturally early, coarse-grained orthopyroxene and corundum and coarse-grained sillimanite mantled by sapphirine + cordierite symplectites is consistent with a clockwise P–T path for the Kemp Land terrane during the Rayner Orogeny. (U + Th)–Pb chemical dating of monazite in peak metamorphic assemblages in metapelites indicates that peak P–T conditions along the coast were coeval at *c.* 940–930 Ma. Recrystallization of monazite may have occurred during high-T metamorphism over *c.* 25 Myr. The observed post-peak microstructures in both Si-saturated and Si-undersaturated rocks from the Stillwell Hills are consistent with a decompressive-cooling P–T path, which contrasts with steep, near-ITD P–T paths that are generally cited for the region. This revised P–T–t path for Kemp Land has implications for tectonic models of mid- to lower crustal response to collisional orogenesis during the Rayner Orogeny. The calculation of pseudosections in chemically realistic systems is currently the most powerful tool for the reconciliation of microstructural evidence from rocks with various bulk compositions. Quantitative P–T paths derived in this way may be (significantly) displaced from P–T trajectories inferred from semi-quantitative petrogenetic grids and geothermobarometry. Our integrated metamorphic and geochronological approach is generally and widely applicable to deciphering the temporal and spatial architecture of metamorphic terranes.

ACKNOWLEDGEMENTS

This work was completed with funding from the Antarctic Science Advisory Committee (G.L.C.: ASAC Project No. 1150) and an ARC Discovery Project (R.W.W. and G.L.C.: DPO552013). Samples were collected during the 1996–1997 and 1997–1998 Australian National Antarctic Research Expeditions. The authors would like to thank the Australian Antarctic Division and the personnel of Mawson Base for their logistic support. Nigel Kelly, Julie Hollis, Chris Carson, Richard White and Vanessa Bennett are thanked for the collection of samples. We are grateful to Ian Kaplin of the EMU at Sydney University for his help with SEM imaging, Barry Searle of the EMU at University of NSW for overseeing data acquisition at the EMP, the Adelaide Microscopy group for their help with EMP monazite dating, and Roger Powell for discussion. J.A.H. was supported by an Australian Postgraduate Award at the University of Sydney. The authors would also like to thank C. J. Carson, A. Zeh and S. L. Harley for their constructive reviews, and R. Gieré for editorial assistance.

SUPPLEMENTARY DATA

Supplementary data for this paper are available at *Journal of Petrology* online.

REFERENCES

Ayers, J. C., Miller, C., Gorisch, B. & Milleman, J. (1999). Textural development of monazite during high-grade metamorphism: Hydrothermal growth kinetics, with implications for U, Th–Pb geochronology. *American Mineralogist* **84**, 1766–1780.

Bingen, B. & van Breemen, O. (1998). U–Pb monazite ages in amphibolite- to granulite-facies orthogneiss reflect hydrous mineral breakdown reactions: Sveconorwegian Province of SW Norway. *Contributions to Mineralogy and Petrology* **132**, 336–353.

Black, L. P., Harley, S. L., Sun, S. S. & McCulloch, M. T. (1987). The Rayner Complex of East Antarctica: complex isotopic systematics within a Proterozoic mobile belt. *Journal of Metamorphic Geology* **5**, 1–26.

Boger, S. D. & White, R. W. (2003). The metamorphic evolution of metapelitic granulites from Radok Lake, northern Prince Charles Mountains, east Antarctica; evidence for an anticlockwise P–T path. *Journal of Metamorphic Geology* **21**, 285–298.

Cherniak, D. J., Watson, E. B., Grove, M. & Harrison, T. M. (2004). Pb diffusion in monazite: a combined RBS/SIMS study. *Geochimica et Cosmochimica Acta* **68**, 829–840.

Clark, C., Mumm, A. S. & Faure, K. (2005). Timing and nature of fluid flow and alteration during Mesoproterozoic shear zone

formation, Olary Domain, South Australia. *Journal of Metamorphic Geology* **23**, 147–164.

Clarke, G. L. (1988). Structural constraints on the Proterozoic reworking of Archaean crust in the Rayner Complex, MacRobertson and Kemp Land coast, East Antarctica. *Precambrian Research* **40–41**, 137–156.

Clarke, G. L., Daczko, N. R. & Nockolds, C. (2001). A method for applying matrix corrections to X-ray intensity maps using the Bence–Albee algorithm and Matlab. *Journal of Metamorphic Geology* **19**, 635–644.

Cocherie, A., Legendre, O., Peucat, J. J. & Kouamelan, A. N. (1998). Geochronology of polygenetic monazites constrained by *in situ* electron microprobe Th–U–total lead determination: implications for lead behaviour in monazite. *Geochimica et Cosmochimica Acta* **62**, 2475–2497.

Crowley, J. L. & Ghent, E. D. (1999). An electron microprobe study of the U–Th–Pb systematics of metamorphosed monazite: the role of Pb diffusion vs overgrowth and recrystallization. *Chemical Geology* **157**, 285–302.

DeWolf, C. P., Belshaw, N. & O'Nions, R. K. (1993). A metamorphic history from micron-scale $^{207}Pb/^{206}Pb$ chronometry of Archean monazite. *Earth and Planetary Science Letters* **120**, 207–220.

Droop, G. T. R. (1987). A general equation for estimating Fe^{3+} concentrations in ferromagnesian silicates and oxides from microprobe analyses, using stoichiometric criteria. *Mineralogical Magazine* **51**, 431–435.

Dunkley, D. J., Clarke, G. L. & Harley, S. L. (1999). Diffusion metasomatism in silica-undersaturated sapphirine-bearing granulite from Rumdoodle Peak, Framnes Mountains, east Antarctica. *Contributions to Mineralogy and Petrology* **134**, 264–276.

Dunkley, D. J., Clarke, G. L. & White, R. W. (2002). Structural and metamorphic evolution of the mid–late Proterozoic Rayner Complex, Cape Bruce, East Antarctica. In: Gamble, J. A., Skinner, D. N. B. & Henrys, S. (eds) *Antarctica at the Close of a Millennium. Proceedings of the 8th International Symposium on Antarctic Earth Sciences. The Royal Society of New Zealand Bulletin*. Wellington: The Royal Society of New Zealand, pp. 31–42.

Ellis, D. J. (1983). The Napier and Rayner Complexes of Enderby Land, Antarctica—contrasting styles of metamorphism and tectonism. In: Oliver, R. L., James, P. R. & Jago, J. B. (eds) *Antarctic Earth Science*. Cambridge: Cambridge University Press, pp. 20–24.

Fitzsimons, I. C. W., Kinny, P. D., Wetherley, S. & Hollingsworth, D. A. (2005). Bulk chemical control on metamorphic monazite growth in pelitic schists and implications for U–Pb age data. *Journal of Metamorphic Geology* **23**, 261–277.

Goncalves, P., Nicollet, C. & Montel, J.-M. (2004). Petrology and *in situ* U–Th–Pb monazite geochronology of ultrahigh-temperature metamorphism from the Andriamena Mafic Unit, north–central Madagascar. Significance of a petrographical *P–T* path in a polymetamorphic context. *Journal of Petrology* **45**, 1923–1957.

Grew, E. S., Manton, W. I. & James, P. R. (1988). U–Pb data on granulite facies rocks from Fold Island, Kemp Coast, east Antarctica. *Precambrian Research* **42**, 63–75.

Halpin, J. A., Gerakiteys, C. L., Clarke, G. L., Belousova, E. A. & Griffin, W. L. (2005). *In-situ* U–Pb geochronology and Hf isotope analyses of the Rayner Complex, east Antarctica. *Contributions to Mineralogy and Petrology* **148**, 689–706.

Hand, M., Dirks, P. H. G. M., Powell, R. & Buick, I. S. (1992). How well established is isobaric cooling in Proterozoic orogenic belts? An example from the Arunta Inlier, central Australia. *Geology* **20**, 649–652.

Harley, S. L. & Hensen, B. J. (1990). Archaean and Proterozoic high-grade terranes of East Antarctica (40–80°C): a case study of diversity in granulite facies metamorphism. In: Ashworth, J. R. & Brown, M. (eds) *High-temperature Metamorphism and Crustal Anatexis*. London: Unwin Hyman, pp. 320–370.

Hawkins, D. P. & Bowring, S. A. (1997). U–Pb systematics of monazite and xenotime: case studies from the Paleoproterozoic of the Grand Canyon, Arizona. *Contributions to Mineralogy and Petrology* **127**, 87–103.

Hensen, B. J. (1988). Chemical potential diagrams and chemographic projections: applications to the sapphirine granulites from Kiranur and Ganguvarpatti. Evidence for rapid uplift in the South Indian Shield? *Neues Jahrbuch für Mineralogie, Abhandlungen* **158**, 193–210.

Holland, T. J. B. & Powell, R. (1998). An internally consistent thermodynamic data set for phases of petrological interest. *Journal of Metamorphic Geology* **16**, 309–343.

Holland, T. J. B., Babu, E. V. S. S. K. & Waters, D. J. (1996). Phase relations of osumilite and dehydration melting in pelitic rocks: a simple thermodynamic model for the KFMASH system. *Contributions to Mineralogy and Petrology* **124**, 383–394.

Indares, A. & Martignole, J. (1985). Biotite–garnet geothermometry in the granulite facies: the influence of Ti and Al in biotite. *American Mineralogist* **70**, 272–278.

James, P. R., Ding, P. & Rankin, I. (1991). Structural geology of the early Precambrian gneisses of northern Fold Island, Mawson Coast, East Antarctica. In: Thomson, M. R. A., Crame, J. A. & Thomson, J. W. (eds) *Geological Evolution of Antarctica*. Cambridge: Cambridge University Press, pp. 19–23.

Johnston, T. E., Brown, M. & Solar, G. S. (2003). Low-pressure subsolidus and suprasolidus phase equilibria in the MnNCKFMASH system: constraints on conditions of regional metamorphism in western Maine, northern Appalachians. *American Mineralogist* **88**, 624–638.

Kamenev, E. N. (1972). Geological structure of Enderby Land. In: Adie, R. J. (ed.) *Antarctic Geology and Geophysics*. Oslo: International Union of Geological Sciences (IUGS), pp. 579–583.

Kelly, N. M. & Harley, S. L. (2004*a*). Orthopyroxene–corundum in Mg–Al-rich granulites from the Oygarden Islands, east Antarctica. *Journal of Petrology* **45**, 1481–1512.

Kelly, N. M. & Harley, S. L. (2004*b*). Inheritance and partial resetting of monazite and xenotime during polyphase metamorphism at granulite and amphibolite facies conditions—an integrated SEM–SIMS–EMP study. *EOS Transactions, American Geophysical Union* **85**(17). Joint Assembly Supplement, Abstract V21D-03.

Kelly, N. M., Clarke, G. L., Carson, C. J. & White, R. W. (2000). Thrusting in the lower crust: evidence from the Oygarden Islands, Kemp Land, East Antarctica. *Geological Magazine* **137**, 219–234.

Kelly, N. M., Clarke, G. L. & Fanning, C. M. (2002). A two-stage evolution of the Neoproterozoic Rayner Structural Episode; new U–Pb sensitive high resolution ion microprobe constraints from the Oygarden Group, Kemp Land, East Antarctica. *Precambrian Research* **116**, 307–330.

Kelly, N. M., Clarke, G. L. & Fanning, C. M. (2004). Archaean crust in the Rayner Complex of east Antarctica: Oygarden Group of islands, Kemp Land. *Transactions of the Royal Society of Edinburgh: Earth Sciences* **95**, 491–510.

Kelsey, D. E., Powell, R., Wilson, C. J. L. & Steele, D. A. (2003*a*). (Th + U)–Pb monazite ages from Al–Mg-rich metapelites, Rauer Group, East Antarctica. *Contributions to Mineralogy and Petrology* **146**, 326–340.

Kelsey, D. E., White, R. W. & Powell, R. (2003*b*). Orthopyroxene–sillimanite–quartz assemblages: distribution, petrology,

quantitative P–T–X constraints and P–T paths. *Journal of Metamorphic Geology* **21**, 439–453.

Kelsey, D. E., White, R. W., Powell, R., Wilson, C. J. L. & Quinn, C. D. (2003*c*). New constraints on metamorphism in the Rauer Group, Prydz Bay, east Antarctica. *Journal of Metamorphic Geology* **21**, 739–759.

Kelsey, D. E., White, R. W., Holland, T. J. B. & Powell, R. (2004). Calculated phase equilibria in K_2O–FeO–MgO–Al_2O_3–SiO_2–H_2O for sapphirine–quartz-bearing mineral assemblages. *Journal of Metamorphic Geology* **22**, 559–578.

Kelsey, D. E., White, R. W. & Powell, R. (2005). Calculated phase equilibria in K_2O–FeO–MgO–Al_2O_3–SiO_2–H_2O for silica-undersaturated sapphirine-bearing mineral assemblages. *Journal of Metamorphic Geology* **23**, 217–239.

Kinny, P. D. (1997). *Users guide to U–Th–Pb dating of titanite, perovskite, monazite and baddeleyite using the W.A. SHRIMP, School of Physical Sciences, Curtin University of Technology*. Perth: Curtin University of Technology.

Kleeman, U. & Reinhardt, J. (1996). Garnet–biotite thermometry revisited: the effect of Al^{VI} and Ti in biotite. *European Journal of Mineralogy* **6**, 925–941.

Marmo, B. A., Clarke, G. L. & Powell, R. (2002). Fractionation of bulk rock composition due to porphyroblast growth: effects on eclogite facies mineral equilibria, Pam Peninsula, New Caledonia. *Journal of Metamorphic Geology* **20**, 151–165.

McLeod, I. R., Trail, D. S., Cook, P. J. & Wallis, G. R. (1966). Geological work in Antarctica; January to March, 1965. *Bureau of Mineral Resources, Australia Record* **1966/9.**

Mezger, K. & Cosca, M. A. (1999). The thermal history of the Eastern Ghats Belt (India) as revealed by U–Pb and $^{40}Ar/^{39}Ar$ dating of metamorphic and magmatic minerals: implications for the SWEAT correlation. *Precambrian Research* **94**, 251–271.

Mikhail, E. M. (1976). *Observations and Least Squares*. New York: Dun–Donelly.

Montel, J.-M., Foret, S., Veschambre, M., Nicollet, C. & Provost, A. (1996). Electron microprobe dating of monazite. *Chemical Geology* **131**, 37–53.

Montel, J.-M., Kornprobst, J. & Vielzeuf, D. (2000). Preservation of old U–Th–Pb ages in shielded monazite: example from the Beni Bousera Hercynian kinzigites (Morocco). *Journal of Metamorphic Geology* **18**, 335–342.

Nair, R. & Chacko, T. (2002). Fluid-absent melting of high-grade semipelites: P–T constraints on orthopyroxene formation and implications for granulite genesis. *Journal of Petrology* **43**, 2121–2142.

Ouzegane, K., Guiraud, M. & Kienast, J. R. (2003). Prograde and retrograde evolution in high temperature corundum-granulites (FMAS and KFMASH systems) from In Ouzzal terrane (NW Hoggar, Algeria). *Journal of Petrology* **44**, 517–545.

Owada, M., Osanai, Y., Toyoshima, T., Tsunogae, T., Hokada, T., Crowe, W. A. & Kagami, H. (2003). Early Proterozoic tectonothermal events in the Napier Complex, east Antarctica: Implications for the formation of East Gondwana. *Gondwana Research* **6**, 231–240.

Parrish, R. (1990). U–Pb dating of monazite and its application to geological problems. *Canadian Journal of Earth Science* **17**, 1431–1450.

Peterson, J. W., Chacko, T. & Kuehner, S. M. (1991). The effect of fluorine on the vapour-absent melting of phlogopite + quartz: implication for deep-crustal processes. *American Mineralogist* **76**, 470–476.

Poitrasson, F., Chenery, S. & Bland, D. J. (1996). Contrasted monazite hydrothermal alteration mechanisms and their geochemical implications. *Earth and Planetary Science Letters* **145**, 79–96.

Powell, R. & Holland, T. J. B. (1988). An internally consistent dataset with uncertainties and correlations: 3. Applications to geobarometry, worked examples and a computer program. *Journal of Metamorphic Geology* **6**, 173–204.

Powell, R., Hergt, J. & Woodhead, J. (2002). Improving isochron calculations with robust statistics and the bootstrap. *Chemical Geology* **185**, 191–204.

Pyle, J. M., Spear, F. S., Cheney, J. T. & Layne, G. (2005). Monazite ages in the Chesham Pond Nappe, SW New Hampshire, U.S.A.: Implications for the assembly of central New England thrust sheets. *American Mineralogist* **90**, 592–606.

Rickers, K., Mezger, K. & Raith, M. M. (2001*a*). Evolution of the continental crust in the Proterozoic Eastern Ghats Belt, India and new constraints for Rodinia reconstruction: implications from Sm–Nd, Rb–Sr and Pb–Pb isotopes. *Precambrian Research* **112**, 183–210.

Rickers, K., Raith, M. & Dasgupta, S. (2001*b*). Multistage reaction textures in xenolithic high Mg–Al granulites at Anakapalle, Eastern Ghats belt, India: examples of contact polymetamorphism and infiltration-driven metasomatism. *Journal of Metamorphic Geology* **19**, 563–582.

Sack, R. O. & Ghiorso, M. S. (1991). An internally consistent model for the thermodynamic properties of Fe–Mg-titano-magnetite–aluminate spinels. *Contributions to Mineralogy and Petrology* **106**, 474–505.

Sandiford, M. & Wilson, C. J. L. (1984). The structural evolution of the Fyfe Hills–Khmara Bay region, Enderby Land, East Antarctica. *Australian Journal of Earth Sciences* **31**, 403–426.

Schröter, F. C. (2006). Mineral trace element distribution in amphibolite to granulite facies mafic rocks. PhD thesis, University of Sydney, 85 pp.

Shaw, R. K., Arima, M., Kagami, H., Fanning, C. M., Shiraishi, K. & Motoyoshi, Y. (1997). Proterozoic events in the Eastern Ghats Granulite Belt, India: evidence from Rb–Sr, Sm–Nd systematics, and SHRIMP dating. *Journal of Geology* **105**, 645–656.

Sheraton, J. W. & Black, L. P. (1981). Geochemistry and geochronology of Proterozoic tholeiite dykes of East Antarctica: evidence for mantle metasomatism. *Contributions to Mineralogy and Petrology* **78**, 305–317.

Sheraton, J. W., Offe, L. A., Tingey, R. J. & Ellis, D. J. (1980). Enderby Land, Antarctica—an unusual Precambrian high-grade metamorphic terrain. *Journal of the Geological Society of Australia* **27**, 1–18.

Sheraton, J. W., Tingey, R. J., Black, L. P., Offe, L. A. & Ellis, D. J. (1987). Geology of an unusual Precambrian high-grade metamorphic terrane—Enderby Land and western Kemp Land, Antarctica. *Australian Bureau of Mineral Resources Bulletin* **223**, 51 pp.

Stüwe, K. & Powell, R. (1995). P–T paths from modal proportions: application to the Koralm Complex, Eastern Alps. *Contributions to Mineralogy and Petrology* **119**, 83–93.

Suzuki, K., Adachi, M. & Tanaka, T. (1991). Middle Precambrian provenance of Jurassic sandstone in the Mino Terrane, central Japan: Th–U–total Pb evidence from an electron microprobe monazite study. *Sedimentary Geology* **75**, 141–147.

Townsend, K. J., Miller, C. F., D'Andrea, J. L., Ayers, J. C., Harrison, T. M. & Coath, C. D. (2001). Low temperature replacement of monazite in the Ireteba granite, Southern Nevada: geochronological implications. *Chemical Geology* **172**, 95–112.

Trail, D. S. (1970). ANARE 1961 Geological Traverses on the Mac.Robertson Land and Kemp Land Coast. *Bureau of Mineral Resources, Geology and Geophysics Report* **135**, 1–32.

Vernon, R. H. (1996). Problems with inferring P–T–t paths in low-P granulite-facies rocks. *Journal of Metamorphic Geology* **14**, 143–153.

White, R. W., Powell, R., Holland, T. J. B. & Worley, B. (2000). The effect of TiO_2 and Fe_2O_3 on metapelitic assemblages at greenschist

and amphibolite facies conditions: mineral equilibria calculations in the system K_2O–FeO–MgO–Al_2O_3–SiO_2–H_2O–TiO_2–Fe_2O_3. *Journal of Metamorphic Geology* **18**, 497–511.

White, R. W., Powell, R. & Holland, T. J. B. (2001). Calculation of partial melting equilibria in the system Na_2O–CaO–K_2O–FeO–MgO–Al_2O_3–SiO_2–H_2O (NCKFMASH). *Journal of Metamorphic Geology* **19**, 139–153.

White, R. W., Powell, R. & Clarke, G. L. (2002). The interpretation of reaction textures in Fe-rich metapelitic granulites of the Musgrave Block, central Australia: constraints from mineral equilibria calculations in the system K_2O–FeO–MgO–Al_2O_3–SiO_2–H_2O–TiO_2–Fe_2O_3. *Journal of Metamorphic Geology* **20**, 41–55.

White, R. W., Powell, R. & Holland, T. J. B (2007). Progress relating to calculation of partial melting equilibria for metapelites and felsic gneisses. *Journal of Metamorphic Geology* (in press).

Williams, M. L. & Jercinovic, M. J. (2002). Microprobe monazite geochronology: putting absolute time into microstructural analysis. *Journal of Structural Geology* **24**, 1013–1028.

Williams, M. L., Jercinovic, M. J. & Terry, M. P. (1999). Age mapping and dating of monazite on the electron microprobe; deconvoluting multistage tectonic histories. *Geology* **27**, 1023–1026.

Yang, P. & Pattison, D. (2006). Genesis of monazite and Y zoning in garnet from the Black Hills, South Dakota. *Lithos* **88**, 233–253.

Young, D. N. & Black, L. P. (1991). U–Pb zircon dating of Proterozoic igneous charnockites from the Mawson Coast, East Antarctica. *Antarctic Science* **3**, 205–216.

Zeh, A., Klemd, R., Buhlmann, S. & Barton, J. M. (2004). Pro- and retrograde *P–T* evolution of granulites of the Beit Bridge Complex (Limpopo Belt, South Africa): constraints from quantitative phase diagrams and geotectonic implications. *Journal of Metamorphic Geology* **22**, 79–95.

Zhu, X. K. & O'Nions, R. K. (1999*a*). Monazite chemical composition: some implications for monazite geochronology. *Contributions to Mineralogy and Petrology* **137**, 351–363.

Zhu, X. K. & O'Nions, R. K. (1999*b*). Zonation of monazite in metamorphic rocks and its implications for high temperature thermochronology: a case study from the Lewisian terrain. *Earth and Planetary Science Letters* **171**, 209–220.

APPENDIX

Methodology of EMP monazite dating and data processing

Elemental mapping was carried out using 20 kV accelerating voltage and 200 nA beam current. The step size for individual maps was between 2 and 4 μm, depending on the size of the grain. Operating conditions for spot-analyses were 20 kV and 100 nA. Th, U and Pb were analysed on the Th Mα, U Mβ, Pb Mα (for maps) and Pb Mβ (for spot analyses) X-ray lines respectively, using a PET crystal. Y was analysed on the La X-ray line using a LiF crystal during monazite mapping and on a PET crystal during spot-analysis. Background measurement positions were optimized to avoid X-ray line overlaps from other elements. On-line and off-line numerical corrections were performed for unavoidable line interferences. An off-line Ce correction, accounting for the addition of apparent Pb because of a second-order Ce escape peak, reduced Pb concentrations by 100 ppm (Clark *et al.*, 2005). Total counting times of 40 s (Th), 80 s (U) and 160 s (Pb) were used to improve counting statistics and age resolution, and also provide optimal time usage. Concentrations of Si, Al, Y, P, Ca, Ce, La, Nd, Sm, Gd, Dy, Pr and Er were analysed for each spot to facilitate proper PAP matrix correlations and to provide a first-pass of data quality (e.g. contamination by silicates). Huttonite ($ThSiO_4$), UO_2 and NBS824 (Pb glass) standards were used to calibrate Th, U and Pb, respectively. The validity of the monazite *in situ* chemical dating method was confirmed using a monazite age standard (Madagascan monazite, MAD) that was analysed regularly during each analytical session. Repeated analyses of MAD during the course of this study yielded an age of 515 ± 13 Ma (2σ; $n = 37$), compared with the SHRIMP $^{238}U/^{206}Pb$ age of 513·8 ± 3 Ma (Kinny, 1997).

Age calculations use the measured Th, U and Pb contents and involve a multi-stage procedure (Kelsey *et al.*, 2003*a*). First, Th and U and corrected Pb concentrations (ppm = 10 000 × wt %) are used to iteratively solve the age equation

$$0 = a\mathrm{Th}(e^{\lambda^{232\mathrm{Th}}t} - 1) + b\mathrm{U}(e^{\lambda^{238\mathrm{U}}t} - 1) + c\mathrm{U}(e^{\lambda^{235\mathrm{U}}t} - 1) - \mathrm{Pb} \quad (1)$$

assuming no uncertainty on the decay constants (Suzuki *et al.*, 1991), where a, b and c are 'molecular constants' [$a = 208/232$, $b = (0{\cdot}9928 \times 206)/238{\cdot}04$, $c = (0{\cdot}0072 \times 207)/238{\cdot}04$], λ^k are decay constants, t is age (Ma), and Th, U and Pb are measured concentrations (ppm). In this way, an age is derived for each spot analysis. Minimum age uncertainties are calculated for every analysed spot, derived by propagating X-ray counting errors through the age equation, analytical uncertainties (1σ) being taken to be equal to the square root of the total counts. Second, individual ages calculated with equation (1) are processed along with their analytical uncertainties using the following methods to arrive at a final age and uncertainty: (1) weighted least squares (wlsq) code implementing Mikhail (1976); (2) the tanh estimator of age (Powell *et al.*, 2002; Kelsey *et al.*, 2003*a*), which is independent of the structure of data scatter. That is, the tanh estimator is able to adequately process data with a non-Gaussian distribution (Powell *et al.*, 2002).